

A Combined *Spitzer* and *Chandra* Survey of Young Stellar Objects in the Serpens Cloud Core.

E. Winston^{1,2}, S. T. Megeath^{1,3}, S. J. Wolk¹, J. Muzerolle⁴, R. Gutermuth¹, J. L. Hora¹,
L.E. Allen¹, B. Spitzbart¹, P. Myers¹, G. G. Fazio¹

ewinston@cfa.harvard.edu

ABSTRACT

We present *Spitzer* and *Chandra* observations of the nearby (~ 260 pc) embedded stellar cluster in the Serpens Cloud Core. We observed, using *Spitzer's* IRAC and MIPS instruments, in six wavelength bands from 3 to 70 μm , to detect thermal emission from circumstellar disks and protostellar envelopes, and to classify stars using color-color diagrams and spectral energy distributions (SEDs). These data are combined with *Chandra* observations to examine the effects of circumstellar disks on stellar X-ray properties. Young diskless stars were also identified from their increased X-ray emission.

We have identified 138 YSOs in Serpens: 22 class 0/I, 16 flat spectrum, 62 class II, 17 transition disk, and 21 class III stars; 60 of which exhibit X-ray emission. Our primary results are the following: 1.) ten protostars detected previously in the sub-millimeter are detected at $\lambda < 24 \mu\text{m}$, seven at $\lambda < 8 \mu\text{m}$, 2.) the protostars are more closely grouped than more evolved YSOs (median separation : ~ 0.024 pc), and 3.) the luminosity and temperature of the X-ray emitting plasma around these YSOs does not show any significant dependence on evolutionary class. We combine the infrared derived values of A_K and X-ray values of N_H for 8 class III objects and find that the column density of hydrogen gas per mag of extinctions is less than half the standard interstellar value, for $A_K > 1$. This may be the result of grain growth through coagulation and/or the accretion of volatiles in the Serpens cloud core.

Subject headings: infrared: stars — X-rays: stars — stars: pre-main sequence — circumstellar matter

¹Harvard Smithsonian Center for Astrophysics, 60 Garden St., Cambridge MA 02138, USA.

²School of Physics, Science Centre - North, University College Dublin, Belfield, Dublin 4, Ireland.

³Current address: Ritter Observatory, Dept. of Physics and Astronomy, University of Toledo, 2801 W. Bancroft Ave., Toledo, OH 43606, USA.

⁴Steward Observatory, University of Arizona, 933 N. Cherry Ave., Tucson, AZ 85721.

1. Introduction

Surveys of molecular clouds indicate that 60% of young stars form in clusters (Carpenter 2000; Allen et al. 2006; Megeath et al. in prep). It is therefore important to study star formation in clusters to understand the influence of the cluster environment in the process of star and planet formation. Of fundamental importance is the understanding of the spatial structure of clusters, and of the evolution of that structure. Observations with the *Spitzer* and *Chandra* Space Telescopes are of great importance in the study of cluster structure as they provide the means to identify young stellar objects from the protostellar to pre-main sequence phases, and to categorize these objects into the canonical evolutionary classes (class 0/I, II and III (Lada & Wilking 1984)). The number and distribution of sources in each of these classes provides unique information on the distribution of star formation sites, the motion of the stars after they form, and the dynamical state of the cluster at large. From these studies, we can better understand the physical processes that govern the fragmentation of molecular clouds, the ensuing trajectories that the resulting young stars make through the cluster, and the eventual fate of the embedded cluster. Clusters also serve as laboratories for the evolution of young stellar objects, and can be used to study the evolution of disks around young stars and the evolution of hot X-ray emitting plasma commonly found around such stars (see for example: Gutermuth et al. (2005); Haisch et al. (2001); Preibisch & Feigelson (2005); Hernandez et al. (2006))

In this paper, we describe a detailed study of the population of young stellar objects in the Serpens cluster identified by observations with *Spitzer* and *Chandra*. The Serpens region is an example of a very young, deeply embedded cluster, containing a number of protostars (Harvey et al. 2006; Hurt & Barsony 1996; Eiroa et al. 1992, 2005; Kaas et al. 2004; Testi et al. 2000). The embedded cluster is heavily extinguished, with a peak extinction exceeding 40 magnitudes in the visual. At a distance of ~ 260 pc, the Serpens cloud core is one of the nearest regions of clustered star-formation to the Sun (see Straižys et al. (2003) for a discussion of the distance to Serpens). This makes it an excellent candidate for study with *Spitzer* as it is close enough to both resolve the individual members and to detect the lowest mass members to below the hydrogen-burning limit. Furthermore, the Serpens cluster is rich in protostars. Sub-millimetre and millimetre observations of the region, at $450 \mu\text{m}$, $850 \mu\text{m}$ and 3 mm, identify at least 14 objects in the Serpens Cloud Core (Testi et al. 1998, 2000; Davis et al. 1999; Hogerheijde et al. 1999; Harvey et al. 2006). In this paper, we extend the sample of known young stellar objects in Serpens using the high sensitivity of *Spitzer* and *Chandra*. We then discuss three topics: the mid-IR spectral energy distributions of protostellar objects detected in the sub-millimeter, the spatial distribution of the Serpens cluster members, and finally, the X-ray properties of the young stellar objects as a function of their evolutionary class.

2. IRAC & MIPS Data Reduction

We have obtained *Spitzer* images of the Serpens Cloud Core in six wavelength bands: the 3.6, 4.5, 5.8 and 8.0 μm bands of the InfraRed Array Camera (IRAC; Fazio et al. (2004)) and the 24 μm and 70 μm bands of the Multi-band Imaging Photometer for *Spitzer* (MIPS; Rieke et al. (2004)). The photometry extracted from these data was supplemented by *J*, *H* and *K_S*-band photometry from the 2MASS point source catalog (Skrutskie et al. 2006), resulting in data in nine photometric bands spanning 1-70 μm . The uncertainties for the point sources as a function of magnitude are shown in Fig. 1. In the following analysis, only data with uncertainties ≤ 0.2 magnitudes were used. Below, we describe the observations, image reduction and photometry for the *Spitzer* data.

2.1. IRAC:

The *Spitzer* Space Telescope has observed the Serpens cluster with the IRAC instrument at two different epochs. The first epoch was on 1st April 2004; these observations were part of the Guaranteed Time Observation program PID 6, *The Structure and Incidence of Embedded Clusters*. The second epoch was on 5th April 2004, during which *Spitzer* executed observations from PID 174 from the *cores to disks* (c2d) legacy program. The mosaicked regions cover a $29' \times 33'$ field in all four of the IRAC wavelength bands (Fig.2). The field is centered on the main Serpens cluster in the Northern Cloud Core. The observations were taken in the high dynamic range mode with a 12 second frame time. In each epoch, two dithered 10.4 second frames and two dithered 0.4 second frames were obtained at each map position.

The analysis used the basic calibrated data (BCD) FITS images from the S11.4 pipeline of the *Spitzer* Science Center. These data were combined into mosaics using the MOPEX program. The 3.6 μm and 4.5 μm images were pre-processed by using the IDL-based pull-down corrector by Lexi Moustakas ¹, and then additional interactive processing steps were applied to locate and remove the remaining column pulldown and mux bleed artifacts in the 3.6 μm and 4.5 μm images, and banding effects in the 5.8 μm and 8.0 μm images (Hora et al. 2004). The overlap correction module was used to minimize instrumental offsets between adjacent frames, and the mosaics were constructed on a pixel scale of 0.8627 "/pixel, or $1/\sqrt{2}$ the IRAC pixel size. The typical total integration time is 41.6 seconds per pixel, although in some regions near the edges of the mosaic, the integration time is 20.8 seconds. The cali-

¹<http://ssc.spitzer.caltech.edu/irac/pulldown/>

bration uncertainty across the IRAC bands is estimated at 0.02 mag (Reach et al. 2005). In addition, there are $\sim 5\%$ position dependent variations in the calibration of point sources in the flat-fielded BCD data; these have not been corrected for in our data. Furthermore, these systematic uncertainties have not been added into the random photometric uncertainties reported in this paper.

We used a custom IDL program for point source finding; this program was a heavily modified version of the DAOfind program in the IDLPHOT package (Landsman 1989). This program first creates a smoothed version of the mosaic by convolving with a Gaussian with $\sigma = 4$ pixels, approximately double the FWHM of the point sources, and then subtracts the smoothed version from the mosaic to filter out the extended nebulosity. The noise in a 8×8 pixel region around the source was calculated to assess the combined instrumental noise, shot noise and noise from the spatially varying extended nebulosity. Point sources with peak values more than 5σ above the background were considered candidate detections. After the point sources were identified, aperture photometry then was obtained using the aper.pro program in the IDLphot package. An aperture radius of 2.8 pixels (2.4") was used, and a sky annulus from 4.2 to 8.4 pixels (3.6" to 7.2") was used to measure the contribution from extended emission in the aperture. The zero points for these apertures were, 17.8204, 17.3025, 16.7408, and 15.9440 mag for the 3.6, 4.5, 5.8, and 8.0 μm bands, respectively, in the native BCD image units of MJy pixels sr^{-1} .

There were 25853, 22703, 6595, and 3946 detections in the 3.6, 4.5, 5.8, and 8.0 μm respectively, with uncertainties less than 0.2 mag, with 2758 of these detected in all four IRAC bands. The sensitivity of the 8.0 μm band is the limiting factor in four band detections: it suffers from lower photospheric fluxes, higher background emission, and the presence of bright, structured nebulosity in some parts of the image. The detection threshold in the 3.6 μm band was 17 magnitudes - far below the hydrogen burning limit for a 1 Myr old star at the distance of Serpens (~ 12 mag at 3.6 μm (Baraffe 1998)).

2.2. MIPS:

Spitzer observed the Serpens cluster twice with the Multiband Imaging Photometer for *Spitzer* (MIPS; Rieke et al. 2004). In both epochs, the medium scan rate was used. For the first epoch, part of the Guaranteed Time Observation program PID 6, taken on the 6th April 2004, six 0.5 degree scan legs with full-array cross-scan offsets were used. For the second epoch observations (PID 174), 12th April 2005, 12 scan legs of length 0.5 degrees and half-array cross-scan offsets were used. In both epochs, the total map size was approximately 0.5 x 1.5 degrees including the overscan region. All three MIPS bands are taken simultaneously

in this mode; because the data at 160 micron are saturated, we do not consider it in our subsequent analysis. The 2nd epoch map had full 70 μm coverage, while the first epoch mapped only six 150'' wide bands, covering half of the map. Both epochs were combined to form the final maps. The typical effective exposure time per pixel is about 80 seconds at 24 μm and 40 seconds at 70 μm . The MIPS images were processed using the MIPS instrument team Data Analysis Tool, which calibrates the data and applies a distortion correction to each individual exposure before combining into a final mosaic (Gordon et al. 2005). The data were further processed using various median filters to remove saturation effects and column-dependent background structure. The resulting mosaics have a pixel size of 1.25'' at 24 μm and 4.95'' at 70 μm .

Stars in the 24 μm mosaic were then identified using PhotVis (Gutermuth 2005), which searched for all point sources with peaks 5 times the RMS noise. Aperture photometry in a 5 pixel aperture was performed on these sources with PhotVis and the photometry was corrected to a 12 pixel aperture radius, with a sky annulus from 12-15 pixels. Adopting a conversion of 6.711 Jy per $DN s^{-1} pix^{-1}$, multiplying by 1/4 to correct for the smaller mosaic pixels and by 1.146 to correct from a 12 mosaic pixel aperture to an infinite aperture, and using a zero magnitude flux of 7.3 Jy, the aperture photometry was converted to magnitudes. Due to the larger 5'' FWHM of the MIPS 24 μm Point Spread Function (PSF), we performed PSF fitting photometry on all the detected sources using the IDL version of DAOPHOT in the IDLPHOT package. The PSF was generated from six bright (3-6 magnitude) stars in the image; these stars were chosen to be bright and uncontaminated by nebulosity. PSF fitting photometry was then performed on the point source detections using the nstar.pro routine in IDLPHOT. The nstar routine requires the input of aperture photometry. Sky values were taken from an annulus from 12 to 15 pixels. These photometry are then adjusted by fitting the PSF to the image data and scaling accordingly. A total of 269 sources were extracted with uncertainties less than 0.2 mag. Three of the sources, numbers 11, 35, and 36, were saturated at 24 μm . The fits of these data were adjusted by scaling the point spread function manually, subtracting the PSF from the image, and visually inspecting the residual in the wings of the PSF. The tabulated magnitudes produced the lowest apparent residual. Since raising/lowering the magnitudes by 0.1 mag would produce a distinct over/undersubtraction in the residual image, we adopted an uncertainty of 0.1 magnitude for these values.

The 70 μm photometry was extracted from the mosaic using a similar procedure to the 24 μm photometry. Aperture photometry was performed on the sources in a 3.66 pixel aperture, with a sky annulus from 3.66-7.92 pixels. The conversion used was 0.675 Jy per $DN s^{-1} pix^{-1}$, with a factor of 1.927 correcting from a 3.66 pixel to an infinite aperture, and a zero magnitude flux of 0.775 Jy. PSF photometry was not performed on the point sources as there were not enough detections uncontaminated by nebulosity to generate the PSF. The

FWHM of the PSF at 70 μm is 18". The typical uncertainty on the 70 μm flux is 15%.

3. *Chandra* X-ray Data Reduction

The X-ray data were taken from the *Chandra* ANCHORS (AN archive of CHandra Observations of Regions of Star formation²) archive, obsid 4479. The raw X-ray data are dominated by events of non-astrophysical origin. To remove these, the raw data were processed using the *Chandra* X-ray Center’s standard processing version 6.13.2 (July 2005). Using `acis_process_events` on the level 1 events file, a gain correction (conversion from pulse heights to X-ray energy) is applied from CALDB 2.21. The CTI correction for pulse heights distorted by Charge transfer inefficiency and VFaint background cleaning to remove soft cosmic rays were also applied. Next an energy filter was applied to remove photons above 8 keV and below 300 eV which are typically not of stellar origin. Finally events with bad grades and bad status (grades 1, 5 and 7, status >0 indicative of X-ray signals) and bad time intervals were filtered using the CIAO tool `dmcoppy`. Time-dependent gain corrections were applied and `acis_process_events` rerun. While there were over 3×10^6 level 1 events, our “cleaned” data file used for analysis contained 171,973 events.

Due to vignetting and small gaps between the chips of the I array the effective collecting area on each part of the sky differs. The effective area also depends on the energy of the photon. The exposure map corrects for the changes in the effective area. An exposure map was created using `merge_all`, accurately representing the average effective area for a 1.7 keV photon. We chose this single energy for the exposure map since it is intermediate between the maximum of the effective area of the HRMA/ACIS system and an estimated mean source energy of ~ 2.0 keV. The exposure map is later applied automatically by CIAO tools extracting count rates and spectra.

3.1. Source Detection

To perform source detection, the data were split into two event lists, one to concentrate on cooler sources with limited noise, consisting of photons with energies between 0.5 and 2.0 keV. The other list contained photons of higher energy between 2.0 and 7.5 keV. WAVDETECT was used for source detection on our cleaned and separated events list to identify sources across the entire I array. Threshold significance was set to detect sources

²<http://cxc.harvard.edu/ANCHORS/>

down to 3.5 sigma and the data were searched on scales of 0.5 to 16". With these settings, a false detection rate of $< 1\%$ is expected. The source detection lists were combined to make a single source list of 88 Sources. IN comparison, Giardino et al. (2006) construct their source list from the same data using different filtering criteria on the bottom 10% of the data. There is $\sim 95\%$ agreement between the two source catalogues.

From the location of the 88 sources, regions were calculated which would contain 95% of the X-ray energy of each sources. The regions are based on the *Chandra* PSF and chip position for each source. The routine *mk_psf* was used to obtain images of the PSF at various off-axis angles θ (arcmin), and rotation angles ϕ (degrees), around the ACIS array. At each source location an ellipse was generated to enclose 95% of the total X-ray energy following Wolk et al. (2006).

3.2. Spectral Analysis

Analysis of the X-ray spectrum of each source was performed to determine the bulk temperature of the corona and the intervening column of hydrogen. For each source with over 25 counts, Source and background pulse height distributions in the total band (0.3-8.0 keV) were constructed. The final fits were done with CIAO version 3.1.0.1 using the CIAO script *psextract* to extract source spectra and to create an Ancillary Response Function (ARF) and Redistribution Matrix Function (RMF) files which correct for the detector response at each location. Model fitting of spectra was performed using *Sherpa* (Freeman et al. 2001). The data for each source were grouped into energy bins which required a minimum of 8 counts per bin and background subtracted. The optimization method was set to Levenberg-Marquardt and χ -Gehrels statistics were employed. An absorbed one-temperature ‘‘Raymond-Smith’’ plasma (Raymond & Smith 1977), was fitted using a two step fitting procedure. Initial conditions were set so that $nH = 1.0 \times 10^{21} \text{cm}^{-2}$ and $kT = 1.0$ keV. Then an initial fit was made with an absorbed thermal blackbody model. These fit results were then used as initial conditions for the absorbed Raymond-Smith plasma model.

4. Band Merging

To generate a catalog of the photometry from all detected sources in the Serpens field, the photometry from the combined IRAC, MIPS and *Chandra* data were merged. In addition, the data were also merged with the 2MASS point source catalog to provide J , H and K_S -band photometry for each detected *Spitzer* source (Skrutskie et al. 2006). Sources observed

in different wavelength bands which were located within $1''$ of each other were considered to be the same source; if while comparing two bands, multiple sources in one of the bands satisfied this criteria, the closest source was chosen.

The field of view (FOV) of each instrument did not cover the same region of the cluster, being most limited by the IRAC FOV in the infrared, and overall by the *Chandra* FOV. The MIPS data covered the entire IRAC field, while the 2MASS survey is not spatially limited. Furthermore, the IRAC detectors are split into two groups, channels 1 & 3 (3.6 & $5.8 \mu m$) and channels 2 & 4 (4.5 & $8.0 \mu m$), whose FOVs are offset from one another by $6.5'$. The field studied in the remainder of this paper is the overlap region of all five *Spitzer* bands, the IR-field (Fig.3). The size of the overlap regions is $26' \times 28'$. In comparison, the *Chandra* image of Serpens covered a $17' \times 17'$ field of view (the IRX-field), centered on the northwestern edge of the cluster, $\sim 2'$ from the center of the IRAC FOV (Fig. 3). X-ray data is not available for all the sources in our catalog.

5. Identification of Young Stellar Objects

The Serpens field contains 19,181 sources with a detection in at least one band with photometric uncertainty < 0.2 in the IR-field (122 having detections in all five bands); however, only a small fraction of these are bona fide YSOs. Three methods were applied to these data to identify possible young stellar objects: selection of stars with IR excesses on IR color-color diagrams, identification of X-ray luminous YSOs by comparison of X-ray sources with IR detections, and finally, a search for extremely red mid-IR sources among the detections.

5.1. Detection by InfraRed Excess

Young stellar objects can be identified by their excess emission at IR wavelengths. This emission arises from reprocessed stellar radiation in the dusty material of their natal envelopes or circumstellar disks. The infrared identification of YSOs is carried out by identifying sources that possess colors indicative of IR excess and distinguishing them from reddened and/or cool stars (Megeath et al. 2004; Allen et al. 2004; Gutermuth et al. 2004; Muzerolle et al. 2004). The main limitation of this method is the contamination from extragalactic sources such as PAH-rich star-forming galaxies and AGN; both of these have colors similar to young stellar objects. Four color-color diagrams were used to determine the color excess of the sources: an IRAC [3.6] - [4.5] vs. [5.8] - [8.0] diagram, an IRAC-MIPS [3.6] -

[4.5] vs. [8.0] - [24] diagram, and two IRAC-2MASS diagrams J - H vs. H - [4.5] and H - K vs. K - [4.5], Fig.4. In the following analysis we required all photometry to have uncertainties < 0.2 mags in all bands used for a *particular* color-color diagram. The numbers of sources for each diagram which satisfy this criteria are 2417, 122, 3748, and 4251, respectively.

5.1.1. IRAC Color-Color Diagram

To identify sources with true IR excesses, it is necessary to distinguish between reddened or cool stars and those with excess emission arising from heated dust grains. A reddening law in the IRAC bands was determined by Flaherty et al.(2006), which shows the [5.8] - [8.0] color to be particularly insensitive to reddening and stellar temperature, and is thus a reliable measure of excess emission due to dust. Sources with a color $> 1\sigma$ beyond $[5.8] - [8.0] > 0.2$ mag are likely to possess excesses and not to be reddened or cool stars (Fig.6).

Extragalactic sources such as PAH rich star-forming galaxies and AGN will also satisfy this criteria (Stern et al. 2005). Sources with a color more than 1σ below $[3.6] - [4.5] < 0.1$ were considered galaxies and were removed; those with a $24\ \mu m$ detection are re-considered separately. Gutermuth et al.(submitted) have recently developed a method for substantially reducing extragalactic contamination built on the Bootes Shallow Survey data (Eisenhardt et al. 2004) and the *Spitzer cores to disks* legacy program methods (Jorgensen et al. 2006; Harvey et al. 2006) . The galaxies are eliminated either by their colors, which unlike YSOs are often dominated by PAH features in the 5.8 and 8.0 μm bands, or by their faintness. AGN are typically much fainter than the YSOs found in nearby star-forming regions and are removed by this criterion. It should be noted that very faint or embedded flat spectrum sources may be erroneously filtered by this method also. Fig.5 shows the color-color and color-magnitude diagrams used to identify star-forming galaxies with strong PAH emission and AGN.

Nebulosity may also result in the misidentification of sources. There are 55 sources with excesses in the [5.8]-[8.0] color, but little evidence of an excess in the [3.6]-[4.5] color. Examination of the spectral energy distributions for these sources (Sec. 6) showed that these sources exhibit excess emission only in the 8.0 μm band. Subsequent analysis showed that seventeen of these also showed excesses in the 24 μm band, but 38 showed no 24 μm detection. The seventeen 24 μm excess sources followed the distribution of the other bona fide YSOs in the field, while the 38 sources with weak 8.0 μm and no 24 μm excess were found in regions of bright 8.0 μm nebulosity to the East of the cluster (Fig. 2). These sources appear to have their 8.0 μm photometry contaminated by the nebulosity and were removed from the sample. In general, all sources with [5.8]-[8.0] excesses which do not show an excess at

24 μm excess or a $[3.6] - [4.5] > 0.1$ are removed.

In total, 146 potential YSOs were identified in the IRAC color-color diagram. Of these, 62 are likely to be contaminants and have been removed from the source list.

5.1.2. IRAC-2MASS Color-Color Diagrams

The shorter wavelength 3.6 and 4.5 μm IRAC bands are much more sensitive to stellar photospheres than the longer wavelength 5.8 and 8.0 μm bands; where the shorter wavelength bands have 17,385 and 15,539 detections with $\sigma \leq 0.2$, respectively, the longer wavelength bands having 4,670 and 2721 detections. Hence many sources cannot be characterized with the IRAC color-color diagram. For this reason, it is important to develop methods to identify sources with infrared excesses that rely only on the shorter wavelength bands. Since we cannot distinguish between reddening and infrared excess from circumstellar dust with only two bands, we combine the near-IR data from the 2MASS point source catalog with the 3.6 and 4.5 μm band photometry (Skrutskie et al. 2006). This provides the ability to detect objects which are too faint for detection in the 5.8 and 8.0 μm bands. In particular, we concentrate on the $J - H$ vs. $H - [4.5]$ diagram and the $H - K$ vs $H - [4.5]$ diagram. These diagrams take advantage of the excellent sensitivity of *Spitzer* in the 4.5 μm band and the stronger infrared excess emission at 4.5 μm compared to that at shorter wavelength (Gutermuth 2005). For highly reddened sources which are not detected in the J -band, the $H - K$ vs. $K - [4.5]$ diagram can be used. It should be noted that the IRAC 3.6 and 4.5 μm data can detect sources too faint or reddened to have been detected by 2MASS. Deeper near-IR imaging is needed to detect these sources in the J , H and K_S -bands.

We calibrated the combined IRAC-2MASS color-color diagrams using a sample of stars which show no evidence for infrared excesses out to 8.0 μm , and which had uncertainties < 0.1 in all IRAC-2MASS bands, c.f. Fig. 6. They were identified primarily by their $[5.8]$ - $[8.0]$ color, which is not significantly affected by extinction (Flaherty et al. 2006). The criteria used were the following:

$$-0.2 < m_{3.6} - m_{4.5} < 1.0 \text{ and } -0.2 < m_{5.8} - m_{8.0} < 0.2$$

The $[3.6]$ - $[4.5]$ color was also limited to values less than one to eliminate contamination from protostars which can have $[5.8]$ - $[8.0]$ close to that of pure photospheres (Hartmann et al. 2005).

This sample of reddened photospheres was then plotted on the $J - H$ v $H - [4.5]$ and

$H - K$ vs. $K - [4.5]$ color-color diagrams to define where the reddened photospheres fall in the diagrams (Fig.6). Reddening vectors derived from Flaherty et al. (2006) were placed on the diagrams so that all of the pure photospheres were blueward (to the left) of the vectors. Sources which were more than 1σ redward of the reddening vectors were selected as having an excess.

Using this analysis on the $J - H$ vs. $H - [4.5]$ diagram, the following criteria for infrared excess stars was established:

$$0.912 \times (m_J - m_H - .6 + \sigma_{JH}) + 0.8 + \sigma_{H2} < m_H - m_{4.5}$$

where 0.912 is the slope of the reddening curve. There were 72 sources detected using these criteria, 27 of which are not found with the IRAC color-color diagram. Of the 27, 12 were found to be contaminants.

In the $H - K$ vs. $K - [4.5]$ diagram, the infrared excess stars were identified using the following criteria:

$$0.873 \times (m_H - m_K + \sigma_{HK}) + 0.4 + \sigma_{K2} < (m_K - m_{4.5})$$

where 0.873 is the slope of the reddening curve. There were 50 sources detected via this plot, 8 not detected on the IRAC or $J - H$ vs. $H - [4.5]$ color-color diagrams. Three of the eight were found to be contaminants.

There were 24 sources identified as having an excess on the IRAC-2MASS color-color diagrams that did not have photometry in all the IRAC bands and did not show a [3.6]-[4.5] color excess. In these cases, the observed infrared excess resulted from a discontinuity between the 2MASS and IRAC photometry; such a discontinuity may be the result of time variability or contaminated photometry. These sources were not selected as infrared-excess sources.

To minimize contamination from AGN, sources which lacked 5.8 and 8.0 μm detections and were identified solely in the IRAC-2MASS color-color diagrams were rejected if their 3.6 μm magnitude was fainter than 15 mag. At the distance of Serpens, this magnitude is well below the cutoff of the Hydrogen-burning limit for 1-3 Myr stars (12-13 mag; Baraffe (1998)). From our analysis of the IRAC color-color diagram (sec 5.1.1), sources identified as AGN dominate this region (Fig. 7).

5.1.3. IRAC-MIPS Color-Color Diagram

For young stars with circumstellar disks, the [3.6] - [4.5] vs. [8.0] - [24.] color-color diagram is very sensitive to the IR excess emission from dust at ~ 3 -5 AU (Muzerolle et al. 2004). It is particularly effective at identifying stars with little to no mid-IR excess shortward of $8.0 \mu m$ due to inner holes in their disks. These transition disks appear to be in a state of evolution where the inner disk has been cleared of small dust grains by planets or grain growth (Lin & Papaloizou 1986). We used the following selection criteria:

$$0.4 \leq m_{8.0} - m_{24} \leq 7.0$$

A lower limit of 0.4 mag was used to conservatively eliminate pure photospheres even in the presence of photometric scatter due to nebulosity and source confusion. This criteria also excludes likely extragalactic sources which have colors [8.0] - [24.] > 7.0 (Muzerolle et al. 2004). A total of 75 young stellar objects were identified on these diagrams, 15 of which were not previously identified in the IRAC and IRAC-2MASS color-color diagrams. Three of the fifteen were identified as extra-galactic contaminants.

5.1.4. Completeness

Estimates for the 90% completeness limit of our *Spitzer* photometry were calculated via the method of inserting artificial stars into the mosaics and then employing our detection algorithms to identify them. The 90% completeness estimates were 15.0, 15.0, 14.5, 12.5, 7.5 at 3.6, 4.5, 5.8, 8.0, and $24 \mu m$, respectively, for the IRAC and MIPS photometry.

Fig. 8 plots the histograms and completeness of sources at $3.6 \mu m$. The dashed black line plots the number of $3.6 \mu m$ detections by magnitude. We have also plotted the number of sources which have sufficient signal to noise in the relevant bands that they can be placed on the IRAC, IRAC-MIPS and/or IRAC-2MASS color-color diagrams (upper grey line). These are the sources which can be searched for IR-excesses. The final YSO catalogue sources are also plotted (lower gray line), as are the YSOs detected in X-rays (lower light gray line). The ratio of the number of sources with $m_{3.6} \leq 15$ mag. that can be placed on the color-color diagrams to the total number of sources with $m_{3.6} \leq 15$ mag. (and correcting this number for completeness by dividing by the fraction of artificial stars recovered in each magnitude bin) is 4532/5629 or 81%.

The same ratio for detections above 14.5 and 14 magnitudes, the percentages are 93% and 97% respectively. These fractions represent lower limits on the completeness of the

YSOs, as the number of contaminating field stars is rising with increasing magnitude, while the number of YSOs does not show an equivalent rise. Magnitudes of 14.5 and 15 for IRAC 3.6 μm , correspond to masses of $\sim 0.02 M_{\odot}$ and $\sim 0.03 M_{\odot}$ at 1 Myrs, and $\sim 0.03 M_{\odot}$ and $\sim 0.04 M_{\odot}$ at 3 Myrs (Baraffe 1998). This completeness limit is for pre-main sequence stars with IR-excess emission from circumstellar disks. Since the fraction of sources with IR-excesses varies with mass and age (Lada 1987; Hernandez et al. 2006), the completeness with respect to all pre-main sequence cannot be estimated with the available data.

5.2. II: Extremely Red Mid-IR Sources

Deeply embedded protostars may only be observable at 8.0 or 24 μm , and thus not be detected by the previous methods (Gutermuth et al. 2004). In order that these objects are not overlooked, the SED of each of the 24 μm detections that was not already selected was visually examined. Three sources were identified at 24 μm only, and one source was identified at 8.0 and 24 μm . One of sources detected at 24 μm lies at the position of a known sub-millimetre source, SMM1 (Testi et al. 1998); it is one of the brightest 24 μm sources on our image ($m_{24} = 1.6$) and is also seen at 70 μm . Another source coincides with SMM8 (Testi et al. 1998); this is detected in both 8.0 μm and 24 μm . It is a fainter source, 11.5 mag at 8.0 μm and 6.3 mag at 24 μm . One of the sources is near the (sub)mm source SMM3, and is probably associated with that source. However, given the lack of clear detections in the IRAC-bands and the lack of a clearly identifiable 70 μm counterpart in this crowded region, we consider this 24 μm source a tentative YSO.

The remaining source, detected only at 24 μm , was detected in only one of the two epochs of MIPS observations, and is probably an asteroid.

5.3. III: X-ray Luminous Stars

Young stellar objects may also possess elevated levels of X-ray emission ($L_{Xbol} \sim 10^3 \times L_{X\odot}$) which can be used to distinguish them from field stars (Feigelson & Montmerle 1999; Feigelson & Kriss 1981). We utilize this property to identify YSOs that do not have emission from a dusty disk (evolutionary class III) and would otherwise be indistinguishable from field stars. Protostars (class 0/I) and pre-main sequence stars with disks (class II) with elevated X-ray emission may also be identified. The *Chandra* image of Serpens covered a $17' \times 17'$ field of view centred on the cluster, and X-ray data is not available for all the sources in our catalog, c.f. Table 8.

The *Chandra* observations detected 88 sources in the region, a mix of genuine YSOs and AGN. The coordinates of these sources were matched against the 19,000 IR sources, with 67 matches, or 76%. The lower limit of the X-ray luminosity detectable in Serpens with *Chandra* can be estimated by comparison with the COUP data, see Feigelson et al. (2005), as $\log_{10} L_X \approx 28.1 \text{ ergs s}^{-1}$, assuming a distance of 260 pc to Serpens and an exposure time of 88 ks. We match the X-ray sources with IR analogues to reduce the contamination from AGN; an X-ray source with no IR counterpart is assumed to be AGN contamination.

Of the 67 matches, 40 were IR excess sources previously identified, 3 sources had only been detected in some of the infrared bands and consequently could not be placed on the color-color diagrams used to identify infrared excess sources. The remaining 24 sources did not exhibit an IR-excess. Of the 67 IR matches, 27 of the X-ray luminous stars are not in the list of infrared excess sources. Of these 27 sources, five of the sources with *Chandra* and *Spitzer* detections were identified as probable AGN using the criteria in Sec 5.1.1. An additional two sources which did not show detections in all of the IRAC bands had $3.6 \mu\text{m}$ magnitudes fainter than 15; these seven sources were considered to be contaminating AGN. In total, 60 YSOs were detected in X-rays, 20 of which are new to the YSO catalog. The completeness of the X-ray data can be assessed from Fig. 8; it should be noted that only 78% of the YSOs from class 0/I to transition disk lie in the IRX-field, thus the completeness of the X-ray data is limited partially by the smaller field of view. For $m_{3.6} < 12$ we detect 57% of the YSOs in X-rays, this percentage drops quickly for fainter magnitudes. This corresponds to a mass of $0.18 M_{\odot}$ for an age ≤ 3 Myr and an $A_V = 5$ (Baraffe 1998).

5.4. Summary of Identified Objects

A total of 229 candidate objects were identified in the overlap IR-field through the methods outlined above. A list of 200 candidate members was compiled from the color-color diagrams, 66 were detected in X-rays in the IRX-field, and three as extremely red mid-IR objects. After contaminant removal there remained a total of 138, which we consider to be bona fide young stellar objects. The membership of Serpens is estimated to be more than 97% complete to 14 mag at $3.6 \mu\text{m}$, or $\sim 0.04 M_{\odot}$ at 1 Myrs (Baraffe 1998), for sources with mid-IR excess emission. As will be shown, $\sim 50\%$ of objects in each evolutionary class are detected in X-rays, thus we are likely missing ~ 21 class III members in the IRX-field. By scaling the Harvey et al. (2006) results to our 0.2 deg^2 field, we estimate that there is of order 1 AGB contaminant in our catalogue. We have removed 15 AGN and 13 galaxies with strong PAH-emission features, and estimate that ~ 1 such contaminating object remains in the final source list (Gutermuth et al. submitted). We estimate that 1 or less of the class III sources

may be a dMe contaminant. A list of the coordinates 137 of the sources identified as young stellar objects in the Serpens Cloud Core is given in Table 4 with associated identifiers. The photometry of the sources is given in Table 5. These two tables do not list the photometry for two sources detected only by MIPS, SMM1 and SMM3, whose fluxes are listed in Table 6. Since SMM3 is only clearly detected by Spitzer at $24 \mu m$, we have not included SMM3 in the 138 sources.

6. Evolutionary Classification

The evolutionary state of a young stellar object can be inferred from the *Spitzer* mid-infrared photometry (Allen et al. 2006). The classification of the Serpens sources was carried out using four different diagnostics: mid-IR colors (Allen et al. 2004; Megeath et al. 2004), the slope of the Spectral Energy Distribution (SED) (Gutermuth et al. 2004), the dereddened SED slope, and the shape of the SEDs (as ascertained by visual inspection). Each source was classified as either class 0/I, flat spectrum, class II, transition disk, or class III (Lada & Wilking 1984, see following subsections for the definition of these classes).

Classification of the sources was carried out by first noting their locations on the IRAC, IRAC-2MASS and IRAC-MIPS color-color diagrams and assigning each source a preliminary class (Megeath et al. (2004); Allen et al. (2004); Gutermuth et al. (2005); Muzerolle et al. (2004), see Fig. 9). Typically, the IRAC color-color diagram was used for the initial assignment of the evolutionary class. An exception was made in the case of the transition disk objects which do not always possess an $8.0\mu m$ excess and are most clearly identified by their [8.0] - [24.] color from the IRAC-MIPS diagram.

This was followed by the construction of SEDs for all sources. Examples of the SEDs for the different evolutionary classes are given in Fig.10. For each SED, a slope $\alpha = d\log(\lambda F_\lambda)/d\log(\lambda)$ was calculated. The conversion from magnitudes to fluxes in $W\text{ cm}^{-2}\text{ s}^{-1}$ used the following zero fluxes for the *J*, *H*, *Ks*, [3.6], [4.5], [5.8], [8] and [24] bands respectively: 3.13×10^{-13} , 1.13×10^{-13} , 4.28×10^{-14} , 6.57×10^{-15} , 2.65×10^{-15} , 1.03×10^{-15} , 3.02×10^{-16} , 3.80×10^{-18} . The slope was calculated by a least-squares fit over the available IRAC bands, and where possible IRAC and MIPS. The near-IR magnitudes were not included as they are most susceptible to extinction.

The Serpens cluster contains many deeply embedded members with extinctions reaching $\sim 40 A_V$. For sources with detections in at least two of the near-IR bands, we have measured the extinction using a method developed by Gutermuth (2006). This method uses the extinction law of Flaherty et al (2006) and the YSO loci from Meyer et al. (1997) and

Gutermuth (2006) to determine the extinction and deredden the sources. The slope of the SED of the dereddened source was also measured.

In the majority of cases the SED slope and color-color diagram methods agreed (118, 86%). Where they did not, further examination was undertaken to ascertain where the discrepancy arose: 18 members (14%) were classed differently via the IRAC and the dereddened SED α methods. Visual inspection of these objects was carried out to better distinguish their class. In 17/18 cases the class derived from the dereddened data was the final choice. The remaining two objects were detected at 8.0 and 24 μm , and 24 μm only, and are coincident with known (sub)mm protostars.

6.1. Class 0/I Protostars

Class 0/I sources are protostellar objects surrounded by in-falling dusty envelopes. They are characterized by rising SEDs in the infrared (Lada 1987). The standard criteria, that class 0 sources with $L_{submm}/L_{bol} \geq 5 \times 10^{-3}$ (Andre et al. 1993), cannot be established from the *Spitzer* data. As some known class 0 sources have been detected with *Spitzer* we refer to all sources showing rising SEDs as class 0/I objects (Hatchell et al. submitted). These sources were identified in our data by their rising SEDs ($\alpha > 0.3$; note we used the 3.6-24 μm slope when available, these may be different to the 3.6-8.0 μm slopes listed in Table 5), and by satisfying one of the two following criteria: (Allen et al. 2004; Megeath et al. 2004):

$$m_{3.6} - m_{4.5} > 0.7 \text{ and } m_{5.8} - m_{8.0} > 0.2$$

$$m_{3.6} - m_{4.5} > 0.5 \text{ and } m_{5.8} - m_{8.0} > 1.1$$

There can be some overlap between highly reddened class II sources (stars with disks) and class 0/I objects (Whitney et al. 2003b). To distinguish between these sources, we used the dereddened SEDs. Sources that showed dereddened SEDs that looked like other class II sources were deemed class II. These objects are found in the class 0/I region of the IRAC color-color diagram in Fig. 8. Although all class 0/I objects might be thought of as class II like objects reddened by their protostellar envelopes; the envelope also results in the scattering of a significant component of light in the near and mid-IR (Kenyon et al. 1993; Whitney et al. 2003a; Doppman et al. 2005). In addition, there may be a contribution from thermal emission from the inner envelope. For this reason, class I objects cannot be simply dereddened, and the application of our dereddening algorithm results in SEDs which appear distinctly different than the class II objects (see Fig. 9). In total, 22 class 0/I protostars were identified.

6.2. Flat Spectrum Objects

Flat spectrum sources possess a ‘flat’ SED ($0.3 > \alpha > -0.3$) (Greene et al. 1994), they do not exhibit the steeply rising SED of protostars (class 0/I), but they have too much excess for it to arise simply from a circumstellar disk (class II). Flat spectrum sources are thought to be an intermediate phase between the class 0/I and class II phase where the central star and disk are surrounded by a thin infalling envelope (Calvet et al. 1994). Initially 26 objects were tentatively classified as flat spectrum sources, using the underreddened α , many because they lacked the necessary near-IR bands to further constrain their classification. This class is particularly sensitive to contamination from AGN, as both have similar colors. Each flat spectrum object was individually examined, and where possible its dereddened slope was used, to distinguish between class 0/I ($\alpha_{dered} > 0.3$), class II ($\alpha_{dered} < -0.3$), and flat spectrum, ($-0.3 < \alpha_{dered} < 0.3$). We used the 3.6-24 μm slope for sources with 24 μm detections; in other cases we used the 3.6-8.0 μm slope (α_{IRAC}) given in Table 5. Finally, the locations of all the flat spectrum members were plotted on the IRAC color-color diagram; these sources delineated the boundary between the class 0/I and II objects (Fig. 8). In total, 16 flat spectrum objects were identified.

6.3. Class II

Class II sources are identified by having an $-2.0 < \alpha < -0.3$ (Greene et al. 1994; Andre et al. 1994), and the following mid-IR colors (Allen et al. 2004; Megeath et al. 2004):

$$m_{3.6} - m_{4.5} < 0.7 \text{ and } m_{5.8} - m_{8.0} < 1.1$$

$$m_{3.6} - m_{4.5} < 0.5 \text{ and } m_{5.8} - m_{8.0} > 1.1$$

Note that we have lowered the minimum slope from -1.6 to -2 in order to contain evolved or anaemic disks found in other star forming regions (Lada et al. 2006; Hernandez et al. 2006). The class II members were refined by addition of the reddened class II objects initially classed as protostars: in total 8 sources (6%) were reclassified from class 0/I to class II. Class II sources from the IRAC-2MASS diagrams were distinguished from protostars by their slopes in the available IRAC bands. In total, 62 class II stars were identified.

6.4. Transition Disks

Seventeen sources were plotted that had an excess at 8.0 and/or $24\mu m$ but none at shorter IRAC wavelengths.

$$-0.3 \geq m_{3.6} - m_{4.5} \leq 0.1 \text{ and } 0.5 \leq m_{8.0} - m_{24} \leq 7.0$$

These sources are considered to be transition disk objects, stars with a cleared inner disk but retaining an outer disk starting at a few AU (Muzerolle et al. 2004; McCabe et al. 2006). It is thought that the inner disk might be cleared due to formation of planets or the agglomeration of the dust particles into larger mm-sized grains (Calvet et al. 2002; Lin & Papaloizou 1986; Muzerolle et al. 2004). Those with weaker $m_{8.0} - m_{24}$ excess (< 1.5) may be debris disks (Muzerolle et al. 2004). Identification of these objects by SED slope is unreliable, due to the jump in flux at the longer wavelengths (Fig. 9). Visual examination of the SED must be carried out to verify that they show excess only longward of $8.0 \mu m$. They tend to lie near the lower boundary of the class II region on the IRAC color-color diagram, showing little or no excess on the [3.6] - [4.5] color-axis and varying degrees of excess along the [5.8] - [8.0] color-axis (Fig. 8). They are more reliably identified using the IRAC-MIPS color-color diagram (Fig. 8). In total we find 17 transition disk candidates. An additional 3 sources were initially classed by their mid-IR color excesses as Class II sources, but were identified as transition disk objects from the lack of excess shortward of $24 \mu m$ in their *dereddened* SEDs. These sources appear in the Class II region in the IRAC and IRAC-MIPS color-color diagrams. (Fig. 8). There is a possible source of contamination in the transition disk sources: AGB stars, which have similar colors (Blum et al. 2006), with $0.5 < m_{8.0} - m_{24} < 1.5$. This affects eight of the sources, spectroscopy will be needed to determine whether these sources are contamination or members.

6.5. Class III

Class III objects are pre-main sequence stars which do not have circumstellar disks detectable in the mid-IR. They exhibit colors in the color-color diagrams consistent with reddened photospheres, an SED which approximately follow a Rayleigh-Jeans law (Lada 1987), and exhibit no excess in the mid-IR. In total, 21 of the X-ray identified YSOs were found to be class III. We cannot distinguish between class III stars without elevated X-ray emission and field stars in the line-of-sight. Considering both the smaller field of view of the *Chandra* observations and the fact that only a fraction of young stars show elevated X-ray emission (see the X-ray discussion in Sec 7.4), a substantial number of unidentified class III objects may exist in the cluster. Further spectroscopic information on stars in the field will

be required to positively identify these Class III sources.

7. Discussion

We have identified 138 young stellar objects: 22 class 0/I objects, 16 flat spectrum sources, 62 class II objects, 17 transition disks, and 21 class III objects. In the following discussion we use this sample to address four topics. First, we compare our results to previous studies of the Serpens embedded cluster. Second, we identify *Spitzer* analogs to sub-millimeter sources previously found in this region. Third, we study the spatial distribution of the sources as a function of their evolutionary class. Finally, we discuss the X-ray properties of the YSOs detected in the *Chandra* X-ray observations.

7.1. Previous Infrared and X-ray Studies

Eiroa & Casali (1992) observed the Serpens cluster in the J, H, K, and nbL bands and identified 50 young stellar objects in the region. We match all 50 sources to detections in our overlap region, although an offset of up to $9''$ was needed to identify their counterparts in our data. Of the 50 sources, 34 have been identified as YSOs in our analysis. The remaining sixteen sources were found to have IRAC colors of reddened stellar photospheres without infrared excesses or to have too few bands to classify reliably, and none of these sixteen sources showed X-ray emission. These sources cannot be established as YSOs by our criteria.

A previous study by Kaas et al. (2004) using the ISOCAM instrument on-board ISO, identified 77 cluster members in a 0.13 deg^2 region centred on the Serpens core, at wavelengths of $6.7 \mu\text{m}$ and $14.3 \mu\text{m}$. Of these, 70 matched with a *Spitzer* detection in the IR-region, with the remaining 7 outside of the overlap region but detected in one or more *Spitzer* bands. A maximum offset of $9''$ was used to match the sources to our data. Of the 70 sources, 56 are identified as YSOs in our final catalogue, while the remaining 14 were found to be reddened stellar photospheres without infrared excesses or X-ray detections. These remaining 14 were not identified as YSOs in our analysis. Of the YSOs in common with Kaas, two of our class II objects are classified as class I by Kaas and one of our class III objects is classified as class II by Kaas.

A previous study of the Serpens Core was undertaken in X-rays by Preibisch (2003) and Preibisch (2004) with the XMM-Newton Satellite. In one observation of $\sim 10 \text{ ks}$ and two observations of $\sim 20 \text{ ks}$ each over an energy range of 0.15-5 keV, 47 sources were detected;

4 class I, 2 flat spectrum, and 41 class II young stars. These observations are not as deep as the 88 ks *Chandra* integration, and do not possess as high an angular resolution. We detect a total of 60 X-ray sources in the *Chandra* data, 13 more members than the Preibisch study. Twelve of these newly discovered X-ray sources are class 0/I or flat spectrum sources, indicating that the *Chandra* observations are detecting more deeply embedded X-ray sources.

Eiroa et al. (2005) describes VLA 3.5cm observations of the Serpens Core, identifying 22 sources, thirteen of which matched to infrared counterparts. Nine of these are class 0/I sources including SMM1 and SMM5, one is a flat spectrum, two are class II and one is class III. Three further sources were matched to counterparts detected in one or two bands only. The class III object is detected in the X-ray, thus all thirteen sources have one of our two criteria for membership: an infrared excess and/or an infrared counterpart (with or without an excess) to an X-ray detection. The remaining six sources without infrared counterparts are most likely background sources which are too faint and/or reddened to be detected in the 2MASS or *Spitzer* infrared data. The fluxes of the VLA sources coincident with the protostars detected in the (sub)mm are given in Table 6. Eight of the 13 VLA sources with infrared counterparts have *Chandra* X-ray counterparts as well; hence, 60% of the VLA sources are detected by Chandra. In comparison, in the ρ Ophiuchus core (165 pc), 8/28 or 36% of the VLA sources had both X-ray and infrared counterparts (Gagne et al. 2004). In the Coronet cluster (140 pc), 9/15 or 60% of the Radio sources have been detected in multi-epoch analysis of X-ray data (Forbrich et al. 2006). The measurements are consistent within the statistical uncertainties of the ratios, even though the sensitivities vary substantially; the X-ray detection rates in the Coronet cluster were found in 20 ks observations, while the ρ Oph core observation was nearly 5 times longer.

Giardino et al. (2006) have recently submitted the results of the *Chandra* observations of the Serpens cluster. This work was done in collaboration with our team, and they have reported the evolutionary classes listed in this paper. Table 4, listing the coordinates and identifiers of the YSOs, provides the cross reference for the Giardino et al. (2006) source numbers in the eighth column.

Harvey et al. (2006) presents IRAC observations of the Serpens cloud as part of the *Spitzer* Legacy project "From Molecular Cores to Planet-forming Disks" (c2d; Evans et al. (2003)). The surveyed area covers a much larger field of 0.89 deg^2 than covered in this paper. They identified 257 young stellar objects throughout the field, in two main groupings. One, labeled 'A' in Harvey et al. (2006), is the Serpens main core cluster studied in this paper, the second region, cluster 'B', being about 1° to the south of the main core. An important difference between this work and that of Harvey et al. (2006) is the selection of class III objects. The Harvey et al. (2006) criterion for class III sources required an $\alpha < -1.6$; their

class III objects are sources with weak infrared emission from a disk that we would classify as a weak class II or transition disk object. In contrast, our class III sources are defined as lacking in infrared emission yet exhibit detectable X-ray emission. Bearing this in mind, the numbers of class I, flat spectrum, class II, and class III members identified in their larger field were 30, 33, 163, and 31, respectively.

7.2. Protostars in the Serpens Clusters

The number of young stellar objects identified is 138. There are 38 protostars (22 class 0/I, 16 Flat Spectrum) and 100 pre-main sequence stars (62 class II, 17 transition disks, and 21 class III). Protostellar class 0/I and flat spectrum sources account for 28% of the YSOs detected. The ratio of protostars to pre-main sequence stars with disks is 48%; this high number indicates that Serpens is unusually rich in protostars, and is in agreement with the 56% fraction found in Kaas et al. (2004). Over the entire Serpens cloud, the ratio was found to be 38% (Harvey et al. 2006). In comparison, the fraction of protostars to stars with disks detected with the *Spitzer* Cores to Disks (c2d) survey was 14% in the IC 348 cluster and 36% in the NGC 1333 cluster (Jorgensen et al. 2006), and $\sim 50\%$ in Chameleon II (Porrás et al. 2007).

Previous observations at sub-millimeter and millimeter wavelengths have identified a number of presumably protostellar sources in the Serpens cluster. Studies by Testi et al. (2000), Davis et al. (1999), and Williams & Meyers (1999) identify fourteen objects detected at wavelengths of 3 mm or 850 μm with flux densities greater than 3 mJy beam $^{-1}$, and significance above 5 σ . Table 6 lists these objects with their identifiers, coordinates, and fluxes from the above mentioned papers combined with our *Spitzer* photometry. These are also shown in Fig. 11. We now discuss these sources:

SMM1: At the location of SMM1 we find a bright 24 and 70 μm source. Outflow knots associated with SMM1 are visible in our 4.5 μm IRAC mosaic, and diffuse emission is visible in the 8.0 μm ; however, we do not identify a compact source at this location. This appears to be a unambiguous example of a Class 0 object too deeply embedded to be detected shortward of 24 μm .

SMM2: Two *Spitzer* identified class 0/I sources are found within 13'' of the SMM2 source; these sources appear to be beyond the positional uncertainties in the 3 mm data ($\sim 6''$) and are not coincident with SMM2. There is also 70 μm emission in the region around SMM2, it is not clear which of the three sources (SMM2 and the two class 0/I) contribute to 70 μm emission. Interestingly, there is a faint slightly extended 4.5 μm source

toward the position of SMM2. This suggests that the SMM2 source may be a protostellar source with associated infrared emission, although the lack of 24 μm emission is puzzling.

SMM3: There is a 24 μm source within 2'' of the location of SMM3, which we tentatively assign to it. While there is extended 70 μm emission in the region of SMM3, no point source could be photometered due to flux contamination from nearby bright sources. While there is faint emission towards this source in the IRAC bands, it is confused with image artifacts from neighboring bright sources.

SMM4: There are no sources identified in the IR coincident with SMM4, but two small areas of nebulosity can be seen in the 4.5 μm image. Again, this suggests that a protostellar source may reside in SMM4, but if so, there is a lack of bright 24 μm and 70 μm emission from the source.

SMM5, SMM9, S68Nb, S68Nc and S68Nd: These five sources are associated with the group of four class 0/I objects on the northwestern side of the cluster. In addition, the outflow jet associated with object S68Nc is visible in the IRAC bands. This region has previously been considered devoid of more evolved pre-main sequence stars, however we have identified two class II members in the vicinity.

SMM6, SMM8, SMM10, PS2: There is a flat spectrum source at the position of SMM6 and class 0/I objects at the positions of SMM8, SMM10 and PS2. Recent work by Haisch et al. (2006) identified SMM6 as the primary component of a double system. We do not see the companion in our data, as it is contaminated by the flux from SMM6 itself.

SMM11: While there is no IR counterpart at the position of SMM11 from Testi et al. (1998), a class 0/I object $\sim 20''$ north of its position is detected out to 70 μm . We also note that the peak of SMM11 in the SCUBA 850 μm data is $\sim 10''$ southeast of our class 0/I source and $\sim 8''$ northwest of the Testi source. While it is possible that these are three separate objects, it seems unlikely; the position of this source needs to be re-examined in subsequent submillimeter observations.

Of the fourteen (sub)mm objects, seven correspond directly to sources detected in the IRAC bands, three are detected only with MIPS, and four are not detected at $\lambda \leq 25 \mu\text{m}$. With the exception of SMM11, all of the (sub)millimeter sources are coincident with 70 μm emission; however, the low angular resolution of the 70 μm map (16'') makes it difficult to extract the 70 μm photometry for an individual source. In seven of these sources, the 70 μm flux can be extracted; these fluxes are tabulated in Table 6 and the resulting SEDs are shown in Figure 12. For the remaining sources, the 70 μm emission is too confused to photometer accurately. Three of the fourteen sources have X-ray detections in our data: SMM5, SMM6, and S68Nb. These appear to be Class I sources in that they show bright emission shortward

of $24 \mu\text{m}$; there is no detectable X-ray emission toward the sources with weak or no detected emission shortward of $24 \mu\text{m}$, i.e. the probable Class 0 sources.

7.3. Spatial Distribution

The spatial distribution of young stellar objects in a cluster gives insight into the fragmentation processes leading to the formation of protostellar cores and the subsequent dynamical evolution of the stars as they evolve from the protostellar to the pre-main sequence stage (Allen et al. 2006). Recent work has shown that in many clusters the sources trace the underlying molecular gas distribution (Gutermuth et al. 2005). Kaas et al. (2004) made the first maps of the distribution of class II and class I objects in Serpens, demonstrating that the class I sources were significantly more clustered than the class II sources.

Fig. 13 shows the distribution of young stars as a function of their evolutionary class. This is shown for the sample of IR-excess stars and the sample of X-ray luminous stars. The most significant difference is between the class 0/I and flat spectrum sources, which are concentrated in a narrow filament in the center of the cluster, and the class II sources. Although there is a peak in the class II density in the center of the cluster, the majority of the class II sources, as well as the transition disk and class III sources, are found in an extended halo surrounding the protostars.

The protostars are coincident with the dense molecular ridge mapped by the $850 \mu\text{m}$ SCUBA map of Davis et al. (1999, 2000). The class 0/I and flat spectrum sources concentrated in two groups coincident with the two dominant molecular gas clumps (Fig. 11), confirming the previous work of Testi et al. (2000) and Kaas et al. (2004). These are coincident with the column density peaks of the $850 \mu\text{m}$ map and have size 0.2 pc in diameter. The northern group contains 9 Class 0/I and 1 flat spectrum source, seven of which are found in a region only 0.1 pc in diameter, and 4 class II sources. The southern group contains a mixture of 12 class 0/I, 10 flat spectrum, 16 class II, 1 transition disk, and 5 class III sources in a ~ 0.2 pc diameter region. In the southwestern quadrant of this grouping is a small wishbone shaped sub-grouping. This sub-grouping of stars contains eight stars in an area 0.1 pc in diameter; including three class 0/I objects, one flat spectrum source and four class II sources. The higher fraction of class II sources in the southern group suggests that it is more evolved than the northern group. Finally, the X-ray data shows a grouping of four class III objects in the southwestern quadrant of the cluster within a 0.1 pc diameter region. This grouping is unusual in that it is the only apparent group of class III objects; all of the remaining class III objects are scattered around the cluster. If this is a bona fide group and not a chance alignment, it is of great interest why these objects have dispersed

their circumstellar material.

The spatial distribution of the cluster sources was examined for each of the five evolutionary classes using a nearest neighbour technique. The nearest neighbour distance is the projected distance to the nearest YSO of the same evolutionary class, using the adopted distance of 260 pc. Figure 14 (*left*) shows the distribution of nearest neighbour distance between the members of each class. The class 0/I sources are by far the most densely clustered, with a median separation of 0.024 pc. In comparison, the median nearest neighbor distances of the remaining evolutionary classes are significantly greater: flat spectrum - 0.079 pc, class II - 0.097 pc, transition disks - 0.132 pc and class III - 0.131 pc. The median distances for the flat spectrum and transition disk are biased to higher values by the small numbers (and hence low densities) of these sources. The class III sources mean distance may be biased to a lower values by the limited field of view of the *Chandra* data. These scales are smaller than the 0.12 and 0.25 pc separations for class I and II previously derived from ISOCAM observations (Kaas et al. 2004), which were limited by the lower angular resolution of ISO. Also plotted in Figure 14 are the cumulative distribution curves for the YSOs by class, showing how densely the sources are distributed over the field. A Kolmogorov-Smirnov (K-S) test was performed to ascertain the probability that they are derived from the same parent distribution. The Class I sources are dissimilar to each of the other classes, reflecting their more highly clustered nature (Table 8). The distributions of the four remaining classes are statistically indistinguishable (Table 8).

For each evolutionary class, 10K random distributions of stars were generated, with the number of stars equal to the number of objects in the given evolutionary class. For the class III sources, the randomly distributed stars were constrained to fall within the IRX-field, for all other classes, the random distribution covered the region of the IR-field that contained 90% of the sources. The resulting nearest neighbor distributions of the observed YSOs and the random distributions were compared for each class using the K-S test. The probabilities that the random and observed distributions were drawn from the same parent distribution were calculated for all 10K distributions; the mean values of the probabilities for each class are listed in Table 8.

Our results indicate that the median projected spacing of protostars in Serpens sources is only 5000 AU, and the spacing is as close as 2000 AU in certain regions such as the wishbone and the northern group. The actual physical spacings are probably larger; if we assume the sources are randomly distributed relative to each other, the median spatial separation between sources would be $1.27 \times 5000 = 6350$ AU. If we assume that each protostar will form an $0.5 M_{\odot}$ star, then for dense core densities of 2.5×10^4 and $6 \times 10^5 \text{ cm}^{-3}$ (Jijina et al. 1999; Olmi & Testi 2002), such a protostar would have to accrete from a volume 12,000 and 4000

AU in diameter, respectively. Thus, assuming volume densities typical of dense molecular cores, the accretion volumes would be densely packed if not overlapping.

Is the observed spacing consistent with Jean’s fragmentation? The Jean’s length is given by (Jeans 1928): $\lambda_J = 0.21 \text{ pc } (T/10 \text{ K})^{1/2} (n_{H_2}/10^4 \text{ cm}^{-3})^{-1/2}$. If we set the Jean’s length to be $1.27 \times 0.024 \text{ pc}$, adopt temperatures of 12 and 17 K (Jijina et al. 1999), and solve for the density, the resulting densities are $6 \times 10^5 \text{ cm}^{-3}$ and $8 \times 10^5 \text{ cm}^{-3}$. The observed gas densities range from $2.5 \times 10^4 \text{ cm}^{-3}$ to $6 \times 10^5 \text{ cm}^{-3}$ (Jijina et al. 1999; Olmi & Testi 2002). Thus, the observed median separation is consistent (i.e. within a factor of two) with Jeans fragmentation given the highest observed densities in Serpens. At these highest observed densities, the spacing would also be approximately equal to the radius of a critical Bonner-Ebert sphere ($R = 0.22 \text{ pc } (T/10 \text{ K})^{1/2} (n_{H_2}/10^4 \text{ cm}^{-3})^{-1/2}$) (Ebert 1955; Bonner 1956). In either case, the spacing of objects at the Jeans spacing and Bonner-Ebert radius further indicate that the volumes of gas accreting onto the protostars are tightly packed or overlapping. We note that unlike the case of Teixeira et al. (2006), there is not a well defined peak in the distribution of nearest neighbor separations; many objects are found at separations much smaller than the median separation. This is in keeping with Young et al. (2006) who resolved one of the Teixeira et al. sources into a multiple system.

The close spacing of the protostars raises the possibility that competitive accretion is taking place. In competitive accretions models, several protostars accrete from a common reservoir of gas. These objects compete for gas from the reservoir; this process can lead to a distribution of masses similar to the initial mass function (Bate & Bonnell 2005). In models of competitive accretion, protostars accrete mass through a Bondi-Hoyle accretion at a rate of

$$\dot{M}_\star = 4\pi\rho\frac{(GM_\star)^2}{(c^2 + v^2)^{3/2}}$$

where ρ is the volume density of the gas, M_\star is the instantaneous mass of the accreting protostar, c is the sound speed of the gas and v is the velocity of the star relative to the gas (Bondi & Hoyle 1944; Bonnell & Bate 2006; Shu 1992). Williams & Meyers (2000) measured the velocities of 5 of the protostars in the northern group by using detections in the N_2H^+ ($1 \rightarrow 0$) line coincident with the protostars. The RMS 1-D velocity dispersion of these protostars is 0.26 km s^{-1} , implying a 3-D velocity dispersion of 0.45 km s^{-1} . Assuming a density of $6 \times 10^5 \text{ cm}^{-3}$, a velocity of 0.45 km s^{-1} , and a kinetic temperature of 17 K (implying a sound speed of 0.22 km s^{-1}), for a protostar with a mass of $0.1 M_\odot$, the Bondi-Hoyle accretion rate is $8 \times 10^{-7} M_\odot$ per year, and for a protostar with a mass of $0.5 M_\odot$, the accretion rate is $2 \times 10^{-5} M_\odot$ per year. Given these accretion rates, adopting a protostellar lifetime of 300,000 (Hatchell et al. submitted), and considering that the rate will increase as the object grows in mass, the young protostars in the northern group could accrete a

significant portion of their ultimate mass through Bondi-Hoyle accretion. Consequently, competitive accretion remains a viable process for the formation of stars in the Serpens cluster.

Finally, the close spacing and velocities of the protostars in the northern group suggest that their envelopes could impinge on one another. We note that the 3 mm continuum observations (5.6'' beamsize) of Williams & Meyers (2000) did not resolve the sizes of the protostars in the northern group of Serpens. This does not rule out our previous estimates that the accretion volumes extend 5000 to 10,000 AU; the BIMA measurements may only be sensitive to dense inner regions of the protostars. However, for the present analysis, we use a size of 1000 AU, assuming that the protostars are spheres with diameters just below the angular resolution of the BIMA observations. We follow the analysis in Gutermuth et al. (2005), adopting a mass of $0.5 M_{\odot}$, a velocity of 0.26 km s^{-1} and a peak density for the northern group of seven protostars in a volume 0.1 pc in diameter. The resulting time between collisions for a given object is 200,000 years, less than the protostellar lifetime. Consequently, if the objects in this group remain in bound orbits within this region for 300,000 years, the typical protostellar lifetime (Hatchell et al. submitted), all of the protostars could experience collisions between their envelopes and the envelopes of other protostars in the group.

In summary, Jean's length, Bonner-Ebert sphere and simple volumetric arguments all suggest that the accreting envelopes around the protostars in Serpens are often tightly packed, if not overlapping. We find that for the conditions present in the northern group, the protostars may accrete a significant amount of their mass through Bondi-Hoyle accretion from a common envelope, and competitive accretion may occur within the group. Furthermore, collisions between the sources are likely. In total, our analysis suggests that the interactions between protostars can play an important role in the formation of stars within the dense groups observed in Serpens.

7.3.1. The Substellar Candidates and their Spatial Distribution

Using the models of Baraffe (1998) we calculate the magnitude of the hydrogen burning limit at K-band to be 12.5 mag for an assumed 1 Myr old cluster at a distance of 260 pc to Serpens. Of the 138 sources in Serpens, 34 have K-band detections fainter than 12.5 magnitudes, 2 of which are class 0/I and one flat spectrum. Since we cannot measure the dereddened photospheric luminosities of the class 0/I and flat spectrum objects, these sources are discounted, leaving 31 candidate (23 class II and 8 class III) brown dwarfs members. Harvey et al. (2006) has also identified numerous substellar candidates in the Serpens 'B' cluster to the south of the core. We cannot rule out that these sources are older

objects or objects that appear underluminous for other reasons (Peterson et al. submitted; Slesnick et al. 2004). Searches for brown dwarfs in other regions have shown that infrared spectroscopy is essential to confirm that faint objects are protostellar in nature (Luhman 2001). Assuming that the 23 class II objects were to be positively identified as substellar, this would lead to an upper limit of 23/138 or 17% of the total YSO population being substellar. This would be somewhat higher than the substellar fractions found in Chameleon 1 (5%) and IC348 (8%) (Luhman 1999, 2005), though in agreement with Kaas et al. (2004), who estimate 20% of Serpens sources are substellar.

Interestingly, the spatial distribution of the $m_K > 12.5$ class II objects appears more extended than the brighter class II (Fig. 15). In particular, although smaller in number, the most distant objects north, west, and east of the core of the cluster have $m_K > 12.5$. This may be biased by the high reddening in the centre of the cluster which would preclude detections of faint objects in the near-IR. Using deeper near-IR photometry of the center of the cluster Kaas et al. (1999) also found that sources with dereddened $m_K > 12.5$ were non-centralised. Spectroscopy of the fainter objects is needed to confirm their substellar nature.

7.4. X-ray Characteristics

In recent years many studies have been undertaken to investigate the emission properties of pre-main sequence stars and protostars in the higher energy X-ray region of the spectrum (Wolk et al. 2006; Getman et al. 2005). In developed, hydrogen burning stars, X-ray activity arises from magnetic fields generated as a result of shear between the core radiative zone and the outer convective zone. The process behind the generation of the highly increased levels of emission in young stellar objects remains uncertain; suggested causes being magnetic disk-locking between the star and disk (Hayashi et al. 1996; Isobe et al. 2003; Romanov et al. 2004), accretion onto the star (Kastner et al. 2002; Favata et al. 2003, 2005), and alternative dynamo models for coronal emission (Küker & Rüdiger 1999; Giampapa et al. 1996). In main sequence stars, there is a trend of decreasing X-ray activity with age; this trend has not yet been conclusively shown for pre-main sequence stars. *Chandra* has recently examined the X-ray properties of the Orion Nebula Cluster (ONC), in a project known as the *Chandra* Orion Ultra-Deep Project (COUP). Although the Serpens sample is much smaller than the COUP survey, the analysis of Serpens has the advantage of excellent 3.6-24 μm photometry; observations longward of 4.5 μm are difficult in the center of the ONC due to the bright infrared emission from the molecular cloud. This photometry allows us to accurately ascertain the evolutionary class of each object, and study the dependence of the X-ray properties with

evolutionary state. Only those detections with X-ray count in excess of 100 were considered when examining emission properties to ensure reliable estimates.

Of the 138 identified members, 60 were conclusively shown to exhibit X-ray emission. Nine of the X-ray detections are associated with Class 0/I sources (43% of class 0/I's in IRX-field), a further eight with flat spectrum members (56%). Twenty detections have class II counterparts (45%), while two of the transition disks are detected in X-rays (25%). The remaining 21 sources did not exhibit an IR-excess and were identified as a class III YSO solely on their X-ray emission; hence, 21/138 or 15% of the sources were identified solely by Chandra. There appears to be no evidence that the detection rate depends on evolutionary class; within 1 σ , the detection rates of class 0/I, flat spectrum, and class II sources are identical. The detection rate may be largely a function of the sensitivity of the *Chandra* observations; the majority of T Tauri stars have $\log(L_x/L_{bol}) > \sim -5.0$ (Preibisch et al. 2005) while our sample is complete to $\log(L_x/L_{bol}) > \sim -4.5$. Since we cannot identify class III sources without X-ray emission, we cannot establish the fraction of class III sources detected in X-rays. As we will argue subsequently, the X-ray properties of the class II and III objects appear to be indistinguishable. Assuming that this similarity holds for the fraction of detected sources, then the fraction of class III sources detected is the same as that for the class II objects, and we estimate the total number of class III objects to be ~ 46 . If, further, we take into account that the IRX-field contains only 71% of the class II population, and we assume that the class III sources show a similar spatial distribution, then the total population of class III objects may be as high as 65.

The ratio of the number of X-ray detected pre-main sequence stars with disks (class II and transition disk) to the total number of X-ray detected pre-main sequence stars (Class II, Class III, and transition disk) is found to be $22/(22+21) = 51\%$. The number counts method of Gutermuth et al. (2005) was not applicable here due to the high density of background stars. These values are comparable to the disk fraction of a ~ 2 Myr old cluster (Hernandez et al. 2006); consistent with the suggestion of Kaas et al. (2004) that the class II population of Serpens is 2 Myr old. However, this older age seems odd considering the large number of protostars in this region. In a future paper, we will examine the positions of these objects on the H-R diagram to better determine the age of the Serpens cluster.

Fig.16(a) shows plasma temperature against the column density of Hydrogen in the intervening gas between us and the hot plasma. The class I and flat spectrum sources show column densities five times greater than the class II and III sources, with one exception. This is not surprising since the class 0/I and flat spectrum sources are surrounded by infalling envelopes. The one exception is a class II object with an unusually high column density, this may be a source where an edge-on disk around the star is occulting the hot plasma. There

does appear to be a correlation of plasma temperature with column density: the values of these 26 sources show a Spearman rank coefficient of 0.55. However, the mean values of kT for N_H greater and less than $2 \times 10^{22} \text{ cm}^{-2}$ are $3.13 \pm 0.25 \text{ keV}$ and $2.62 \pm 1.34 \text{ keV}$, respectively, indicating that there is no strong dependence. This indicates that the column density is not biasing our determination of the temperature to higher values by selectively absorbing the soft X-ray flux. Soft X-ray photons are more highly absorbed than hard X-ray photons, by up to 90% when $A_V > 30$ (Feigelson et al. 2005). Further more, it shows that there is no significant trend of plasma temperature with evolutionary class.

Fig.16(c) shows the X-ray flux corrected for absorption and kT for the different classes. Although the class 0/I objects appear slightly more luminous, this may be a bias due to the fact that the class 0/I sources are much more highly absorbed and consequently the weaker class I objects may not have had the 100 counts we require to perform the analysis of the X-ray spectrum. The 8 class II and 9 class III sources have statistically indistinguishable values; the mean values of the class II are $kT = 3.45 \pm 1.31 \text{ keV}$ and $F_X = 1.33 \pm 1.47 \times 10^{13} \text{ erg cm}^{-2} \text{ s}^{-1}$ and the mean value for the class III sources is $kT = 2.38 \pm 0.96 \text{ keV}$ and $F_X = 0.93 \pm 0.77 \times 10^{13} \text{ erg cm}^{-2} \text{ s}^{-1}$. The mean values for the class I are $kT = 3.17 \pm 0.33 \text{ keV}$ and $F_X = 3.22 \pm 2.08 \times 10^{13} \text{ erg cm}^{-2} \text{ s}^{-1}$, for the flat spectrum are $kT = 2.48 \pm 0.47 \text{ keV}$ and $F_X = 2.72 \pm 2.31 \times 10^{13} \text{ erg cm}^{-2} \text{ s}^{-1}$, and for the transition disks are $kT = 0.92 \pm 0.06 \text{ keV}$ and $F_X = 3.92 \pm 1.56 \times 10^{14} \text{ erg cm}^{-2} \text{ s}^{-1}$. Using the combined class II and class III sample we find only some indication of a weak correlation of kT with X-ray flux, with a Spearman rank coefficient of 0.39. In comparison, Jeffries et al. (2006) find a trend of increasing kT with X-ray in a combined study of several young clusters. Finally, the mean plasma temperatures for the class 0/I and flat spectrum sources are not significantly different than those values for class II and class III sources. Thus, we find no significant dependence of plasma temperature on evolutionary class for the detected X-ray sources.

The X-ray flux of pre-main sequence stars has been found to vary with bolometric luminosity (Feigelson et al. 1993; Casanova et al. 1995). Although we cannot measure the bolometric luminosities, we can examine the X-ray flux as a function of the dereddened J-band magnitude, which is the infrared band least contaminated by infrared excess emission and is thus a good proxy for photospheric emission (Fig.16(b)). We find again that the class II and class III sources appear indistinguishable. In particular, if we limit our analysis to dereddened $J < 11$ where we detect 90% of the class II sources in X-rays, we find that the $F_X = 6.26 \pm 3.06 \times 10^{-14} \text{ erg cm}^{-2} \text{ s}^{-1}$ for class II and $F_X = 10.76 \pm 8.15 \times 10^{-14} \text{ erg cm}^{-2} \text{ s}^{-1}$ for class III. A similar lack of dependence is found in NGC 1333 and $\sigma \text{ Ori}$ (Getman et al. 2002; Hernandez et al. 2006). This suggests that the mechanism generating the X-ray flux is similar during the class II and III phases. Getman et al. (2002) find a clear relationship between F_X and J-band magnitude of slope 0.47 ± 0.06 in NGC1333, while Casanova et al.

(1995) find a slope of 0.30 in the Ophiuchi cloud. Our results give a slope of 0.42 ± 0.17 , which is consistent with these other young clusters, although there is a large uncertainty due to the scatter in our data. In conclusion, we find that there is no clear observational motivation for invoking different mechanisms for generating the X-ray emission in the class I, II and III phases.

The combined X-ray and infrared results can be used to calibrate the relationship between gas column density and the extinction measured in the infrared. We calculated A_K for each star using the method of Gutermuth et al. (2004), which is based on the reddening loci from Meyer et al. (1997) and the extinction law of Flaherty et al. (2007). These values can be compared to the column density of hydrogen atoms, N_H , which is calculated from the inferred absorption of the X-ray emission. Previous measurements of this value lead to an approximately linear fit of $1.6 \times 10^{21} A_V$ (Vuong et al. 2003; Feigelson et al. 2005) for stellar sources, while the value for the diffuse ISM ranges from $1.8 - 2.2 \times 10^{21} A_V$ (Vuong et al. 2003; Gorenstein 1975). Fig.16(c) plots the hydrogen column density against the calculated extinction in the K-band. As shown in this plot, the Vuong et al. (2003) relationship agrees with our data for $A_K < 1$, but diverges from the points with $A_K > 1$. A similar divergence has also been found in the more deeply embedded stars in the RCW 108 region (Wolk et al. 2007).

Interestingly, the class II sources always show a higher value of N_H for a given A_K . The colors of the class II objects can be affected by both absorption and scattering of the light from the central source by a flared disk; the extent of this effect would be determined, predominantly, by the inclination of the disk and the sizes of grains in the disk (Whitney et al. 2003b). For example, the colors of an edge-on disk system, where the central star is highly obscured by the disk, would be dominated by scattered light. In such a case, the disk absorbs both the infrared and the X-ray emission from the star, but the scattered infrared light reduces the observed reddening of the star and hence the inferred value of A_K . To eliminate the uncertainties in the determination of A_K due to circumstellar material, we fit only the class III objects. The resulting relationship is $N_H = 0.63 \pm 0.23 \times 10^{22} A_K$. Assuming a standard conversion of $A_K = 0.1 A_V$ (Rieke & Lebofsky 1985), this slope is 2.5 times lower than that derived by previous authors. In comparison, a fit to the class II objects results in $N_H = 1.3 \pm 0.93 \times 10^{22} A_K$. The poor fit and higher slope are further indication that the disks around these objects affect the measurement of A_K , possibly leading to spuriously low values of A_K . We now focus on the slope derived from the class III objects, the possible systematic uncertainties in that slope, and a possible explanation for the low value of the slope.

Systematic underestimation of N_H : If the measurements of N_H were systematically

underestimated by a factor of 2.5, then this would lead to the shallower slope observed. However, the determinations of the N_H values appear to be robust. We calculated N_H only for those sources with relatively high S/N (> 100 counts). These values of N_H were found to be consistent using two different models for the plasma. A bias could occur in the determination of N_H when the soft X-ray emission is totally absorbed; however inspection shows that this is not the case here. Furthermore, values of N_H calculated by our software for stars in the Orion COUP survey are within 5% of the values published in Getman et al. (2005); this is further validation of the accuracy of our analysis.

Systematic overestimation of A_K : The value of A_K is determined by the selective absorption in the near-infrared bands (Gutermuth et al. 2004); this selective absorption was converted to A_K by using an assumed value of $A_K/E(H - K)$. We use the Indebetouw et al. (2005) reddening law where the adopted ratio of $A_H/A_K = 1.55$. This is equivalent to a near-IR general to selective absorption of $A_K/E(H - K) = 1.82$. Changes in the reddening law in the molecular cloud could change this ratio. In molecular clouds, Flaherty et al. (2007) report a flattening in the infrared reddening law for $\lambda > 3.6 \mu m$ compared to the diffuse ISM reddening law measured by Indebetouw et al. (2005); however, they found no significant difference in the reddening law for $\lambda = 1 - 2.1 \mu m$ between the molecular clouds and the diffuse ISM. Alternatively, Nishiyama et al. (2006) report $A_K/E(H - K)$ of 1.44, lower than the value in Indebetouw et al. (2005), and they find evidence of variations in this value toward different lines of sight toward the galactic center. If the slope found in our data were wholly due to an overestimation of A_K , then the value of $A_K/E(H - K)$ would have to decrease to 0.73, and the value of A_H/A_K must change to 2.37. This value of A_H/A_K is higher than the values in the literature and would require a steepening of the reddening law between 1 & 2 μm .

Growth and Coagulation of Dust Grains: The ratio N_H/A_K can be affected by increases in the sizes of dust grains; this would simply increase the value of A_K and hence reduce the ratio of N_H/A_K . The value of A_K is given by:

$$A_K = 1.086 N_d \pi \int a^2 Q_{ext} n(a) da$$

where N_d is the column density of dust, a is the radius of a dust grain, and Q_{ext} is the extinction efficiency (Whittet 2003). In the limit of $\lambda < a$, Q_{ext} , which would be the case for a standard grain size distribution (Mathis et al. 1977) of $n(a) \propto 0.005 < a_d^{-3.5} < 0.25 \mu m$,

$$Q_{ext} = \frac{8\pi a}{\lambda} Im \left\{ \frac{m^2 - 1}{m^2 + 2} \right\} + \frac{8}{3} \left(\frac{2\pi a}{\lambda} \right)^4 \left| \frac{m^2 - 1}{m^2 + 2} \right|^2$$

where m is the refractive index. Thus, there is a strong dependence on the size of the grain, and the value of A_K can be changed simply by growing grains to larger sizes; for example

the scattering term in Q_{ext} goes as $(\frac{2\pi a}{\lambda})^4$, hence a 25% increase in grain size can increase the scattering efficiency by a factor of 2.5.

Grain growth in molecular clouds may occur through both coagulation and the accretion of grain mantles; these processes would be accelerated in the dense molecular gas found in the Serpens cloud core. For example, Jura (1980) explained changes in the N_H/A_V ratio in Ophiuchus through the coagulation of grains. The collision time between grains is (Jura 1980)

$$t_{col} = (10^{-16}n_H[cm^{-3}]v_d[km\ s^{-1}])^{-1}$$

For a $n_H = 10^5 cm^{-3}$ and a velocity of $0.1\ km\ s^{-1}$ (Jura 1980), the collision timescale is 30,000 years. Thus it is likely that a dust grain in the Serpens cloud would have had multiple collisions with other grains. Alternatively, the growth can be through the accretion of mantles of volatiles such as H_2O , NH_3 , O_2 , N_2 and CO . The accretion timescale is given by

$$t_m = \frac{2.5s\Delta a}{Sn(kT_g m)^{\frac{1}{2}}}$$

where s is the specific density of the mantle, Δa is the change in the size of the dust grain due to the mantle, S is the sticking coefficient (~ 1), T_g is the temperature of the gas, n is the density of the molecule forming the mantle, and m is the mass of the molecule forming the mantle (Whittet 2003). Thus the rate of mantle accretion is proportional to the density of the gas; again, the high density of the gas in the Serpens cloud would accelerate the rate of mantle accretion. A detailed calculation of the rate requires consideration of the gas phase abundances of the different possible volatiles, and is beyond the scope of this paper.

Self consistent modeling of the extinction over multiple wavelength bands is needed to study the impact of grain growth on both the relationship between N_H and A_K and the shape of extinction law with which A_K is derived. Further observational work is also needed to confirm our observed N_H/A_K slope using a larger number of class III objects from multiple star forming regions. However, this study demonstrates the value of using combined Chandra, near-IR, and Spitzer observations to identify deeply embedded class III objects and search for variations in the extinction law within molecular clouds.

8. Conclusion

We have undertaken an intensive study of the Serpens Cloud Core in the mid-IR with *Spitzer* and in the near-IR with 2MASS. We have merged these data with *Chandra* X-ray

observations and investigated various X-ray properties of protostars and pre-main sequence stars. These data provide perhaps the most complete census to date of the young stellar objects in one of the nearest embedded clusters to the Sun.

- We identify 138 young stellar objects, after removing contamination. These include 38 protostars (22 class 0/I, 16 Flat Spectrum) and 100 pre-main sequence stars (62 class II, 17 transition disks, and 21 class III). The ratio of protostellar objects (class 0/I and flat spectrum) to pre-main sequence stars (class II, transition disk, and class III) is 38:100 or 29% of the total number of identified members. The ratio of protostars to pre-main sequence stars with disks is 48%. These high numbers indicate that Serpens is unusually rich in protostars. We estimate that as many as 44 class III sources may be missing, implying a total membership of 182.
- We have searched for *Spitzer* counterparts to 14 (sub)mm sources in the Serpens cluster. Seven are detected as point sources at 3.6-8.0 μm , a total of 10 have been detected at 24 μm , and an additional two show nebulosities at $\lambda \leq 24 \mu m$. All but one are coincident with 70 μm emission, although for many of the protostars, the low angular resolution of the 70 μm data precludes accurate photometry of the sources.
- We find that the spatial distribution of the protostars is distinctly different than the pre-main sequence stars. While the class 0/I sources and most of the flat spectrum sources are concentrated in the central molecular gas filament, the class II, transition disk and class III sources are distributed over a much more extended region. The median projected spacing of the Class 0/I sources is only 5000 AU; these sources are highly clustered. In contrast, the distribution of the remaining classes are statistically indistinguishable from a random distribution.
- The protostars are concentrated in two groups coincident with the two dominant molecular gas clumps, as has been previously reported. The density of protostars in these groups suggest that the volumes of gas from which these protostars accrete may touch or overlap. The spacing is also similar to both the Jean's length and the radii of critical Bonner Ebert spheres. Based on published ambient gas densities and velocities of the protostars in the northern group, we find that competitive accretion could be occurring in this groups. Furthermore, collisions between protostellar envelopes may be common.
- Of the 138 sources, 60 exhibit detectable X-ray emission. Nine of the detections are associated with class I sources (43% of members in class), a further eight with flat spectrum members (56%). Twenty-one detections have class II counterparts (45%),

while only two of the transition disks are detected in X-rays (25%). Twenty class III sources were identified solely by their X-ray emission. There appears to be no evidence of a trend in the detection rate of sources by evolutionary class. The fraction of X-ray detected pre-main sequence stars (i.e. class II, transition disks and class III sources) with disks is 51%.

- We find no evidence for a dependence of the temperature of the X-ray emitting plasma on the evolutionary class, and find no difference in the X-ray luminosity of detected class II and class III objects. Consequently, there is no evidence that the generation mechanism of the X-ray emission depends on the presence of an infalling envelope or circumstellar disk.
- We find an observed relationship of $N_H = 0.63 \pm 0.23 \times 10^{22} A_K$, which is much shallower than found in other studies. The most likely explanation for this is a change in the near-IR reddening law that would affect the shape and magnitude of the reddening law. Such changes could result from grain coagulation and/or grain growth from the accretion of mantles of volatiles; both such processes may occur relatively quickly due to the high gas (and presumably dust grain) densities in the Serpens cloud core.

This work is based on observations made with the *Spitzer* Space Telescope (PID 6, PID 174), which is operated by the Jet Propulsion Laboratory, California Institute of Technology under NASA contract 1407. Support for this work was provided by NASA through contract 1256790 issued by JPL/Caltech. Support for the IRAC instrument was provided by NASA through contract 960541 issued by JPL. This publication makes use of data products from the Two Micron All Sky Survey, which is a joint project of the University of Massachusetts and the Infrared Processing and Analysis Center/California Institute of Technology, funded by the National Aeronautics and Space Administration and the National Science Foundation. This research has made use of the NASA/IPAC Infrared Science Archive, which is operated by the Jet Propulsion Laboratory, California Institute of Technology, under contract with the National Aeronautics and Space Administration. E. Winston would like to thank the Irish Research Council for Science, Engineering, and Technology (IRCSET) for funding and support.

REFERENCES

- Allen, L., Calvet, N., D’Alessio, P., et al, 2004, *ApJSS*, 154, 363-366.
- Allen, L. et al., 2006, *Protostars & Planets V*.

- Andre, P., Ward-Thompson, D., & Barsony, M., 1993, *ApJ*, 406, 122-141.
- Andre, P., Montmerle, T., 1994, *ApJ*, 420, 837.
- Armitage, P. J., Clarke, C. J. & Francisco, P. 2003, *MNRAS*, 342, 1139.
- Baraffe, I., 1998, *A&A*, 337, 403,
- Bate, M. R. & Bonnell, I. A. 2005, *MNRAS*, 356, 1201
- Blum, R.D., et al., 2006, *ApJ* , 132, 2034-2045.
- Bondi, H., Hoyle, F., 1944, *Mon. Not. R. Astron. Soc.*, 104, p.273.
- Bonnell, I. A.& Bate, M. R., 2005, *MNRAS*, 362, 915.
- Bonnell, I. A.& Bate, M. R., 2006, *MNRAS*, 370, 488.
- Bonner, W.B., 1956, *MNRAS*, 116, 351.
- Calvet, N., D'Alessio, P., Hartmann, L, Wilner, D, Walsh, A, Sitko, M., 2002, *ApJ*, 568, 1008.
- Calvet, N., Hartmann, L., Kenyon, S.J., Whitney, B.A., 1994, *ApJ*, 434, 330.
- Carpenter, J.M., 2000, *AJ*, 120, 3139-3161.
- Casanova, S., Montmerle, T., Feigelson, E.D., Andre, P., 1995, *ApJ*, 439, 752.
- Davis, C.J., Matthews H.E., Ray T.P., et al, 1999, *Mon. Not. R. Astron. Soc* 309, 141-152.
- Davis, C.J., et al., 2000, *ApJ*, 530, L115-L118.
- Doppman, G.W., Greene T.P., Covey K.R., Lada C.J., 2005, *ApJ*, 130, 1145-1170.
- Ebert, R., 1955, *Z. Astrophys.*, 37, 217.
- Eiroa, C., Casali M., 1992, *A&A*, 262, 468-482.
- Eiroa, C., Torrelles J.M., Curiel S., Djupvik A.A., 2005, *ApJ*, 130, 643-651.
- Eisenhardt, P.R., et al., 2004, *ApJS*, 154, 48.
- Evans, N.J. II, et al., 2003, *Pub. Astron. Soc. Pacific*, 115, 965-980.
- Favata, et al., 2003, *A&A*, 403, 187.

- Favata, et al. , 2005, ApJS, 160, 469.
- Fazio, G.G., et al., 2004, ApJS, 154, 10.
- Feigelson, E., Getman, R., et al., 2005, ApJ, 160.
- Feigelson, E. D., Montmerle, T., 1999, ARA&A, 37, 363-408.
- Feigelson, E.D., Casanova, S., Montmerle, T., Guibert, J., 1993, ApJ, 416, 623.
- Feigelson, E. D.; Kriss, G. A., 1981, ApJ, 248, L35-L38.
- Flaherty, K.M., et al., 2007, ApJ, submitted.
- Forbrich, J., Preibisch Th., & Menten K.M., 2006, A&A, 446, 155-170.
- Freeman, P., Doe, S., Siemiginowska, A., Proc. SPIE Vol. 4477, p. 76-87, Astronomical Data Analysis, Jean-Luc Starck; Fionn D. Murtagh; Eds.
- Gagne, M., Skinner, S. L., Daniel, K. J., 2004, ApJ, 613, 393-415.
- Getman, K. V., et al., 2005, ApJS, 160, 319-352.
- Getman, K. V., et al., 2002, ApJ, 575, 345-377.
- Giampapa, M.S., et al., 1996, ApJ, 463, 707.
- Giardino G., Favata, F., et al., 2007, ApJ (submitted).
- Gordon, K. D., et al. 2005, PASP, 117, 503.
- Gorenstein, P., 1975, ApJ, 198, 95.
- Gutermuth, R., Megeath, S. T., Pipher, J., Williams, J. P., Allen, L., Myers, P., Raines, S. N., 2005, ApJS, 154, 374.
- Gutermuth, R., Megeath, S. T., Muzerolle, J., Allen, L., Pipher, J., Myers, P., Fazio, G. G., 2004, ApJS, 154, 374.
- Gutermuth, R., 2005, PhD Thesis.
- Gutermuth, R., et al., 2007, ApJ (submitted).
- Greene, T.P., Wilking, B.A., Andre, P., Young, E.T., Lada, C.J., 1994, ApJ, 434, 614.
- Haisch, K. E. Jr., Lada, E. A. & Lada, C. J. 2001, ApJ, 553, L153.

- Haisch, K. E. Jr., Barsony, M., Ressler, M.E., Greene, T.P., 2006, *AJ*, 132, 2675-2684.
- Hartmann, L., Megeath, S.T., Allen, L.E., Luhman, K., Calvet, N., D'Alessio, P., Franco-Hernandez, R., Fazio, G., 2005, *ApJ*, 629, 881-896.
- Harvey, P., Chapman N., Lai S-P., 2005, *ApJ*, 644, 30-325.
- Hatchell, J., arXiv:astro-ph/0612601v1.
- Hayashi, M.R., Hibata, K., Matsumoto. R., 1996, *ApJ*, 468, L37.
- Hernandez, J., et al., 2006, submitted to *ApJ*.
- Hogerheijde, M., van Dishoeck E., Salverda J., 1999, *ApJ*, 513, 350-369.
- Hora, J., et al., *Proc. SPIE*, 5487, 77.
- Hurt, R., Barsony M., 1996, *ApJ*, 460, L45-L48.
- Isobe, H., et.al., 2003, *PASJ*, 55, 967.
- Indebetouw, R., Mathis, J.S., Bebler, B.L. et al., 2005, *ApJ*, 619, 931-938.
- Jayawardhana, R., Hartmann, L, Fazio, G, Fishter, R. S., Telesco, C. M., & Pina, R. K. 1999, *ApJ*, 521, L129.
- Jeans, J.H., *Astronomy & Cosmogony*, 1928, The University Press, Cambridge, UK.
- Jeffries, R.D., Evans, P.A., Pye, J.P., Briggs, K.R., 2006, *Mon. Not. R. Astron. Soc.*, 367, 781-800.
- Jijina, J., Myers, P.C., Adams, F.C., 1999, *ApJ Supplement Series*, 125, 161-236.
- Jorgensen, J., Harvey, P., et al, 2006, *ApJ*, 645, 1246-1263.
- Jura, M., 1980, *ApJ*, 235, 63.
- Kaas, A.A., Olofsson G., Bontemps S., et al, 2004, *A&A*, 421, 623-642.
- Kaas, A.A., 1999, *AJ*, 118, 558-571.
- Kastner, J.H., et al., 2002, *ApJ*, 567, 434.
- Kenyon, S. J., Calvet, N., Hartmann, L., 1993, *ApJ*, 414, 676.
- Krumholz, M. R., McKee, C. F., & Klein R. I., 2005, *Nature*, 438, 332.

- Küker, M., & Rüdiger, G., 1999, *A&A*, 346, 922.
- Lada, C.J., Wilking, B.A., 1984, *ApJ*, 287, 610-621.
- Lada, C.J., IAU Symp. 115, 1987, *Star Forming Regions* ed. M Peimbert & J. Jugaku.
- Lada, C.J., et al., 2006, *AJ*, 131, 1574.
- Landsman, W.B., 1989, *Bulletin of Amer. Astron. Society*, Vol. 21, p784.
- Lin, D. N. C., Papaloizou, J., 1986, *ApJ*, 309, 846-857.
- Luhman, K. L. 1999, *ApJ*, 525, 466.
- Luhman, K. L. 2001, *ApJ*, 560, 287.
- Luhman, K.L., 2005, *Protostars and Planets V*.
- Mathis, J.S., Rumpl, W., Nordsiek, K.H., 1977, *ApJ*, 217, 425.
- McCabe, C., Ghez A.M., et al, 2006, *ApJ*, 636, 932-951.
- Megeath, S.T., Gutermuth R.A., Allen L.E., Pipher J.L., Myers P.C., Fazio G.G., 2004, *ApJS*, 154, 367.
- Megeath, S.T., et al., in prep.
- Meyer, M. R.; Calvet, N.; Hillenbrand, L. A., 1997, *AJ*, 114, 288-300.
- Muzerolle, J., Megeath, S., Gutermuth, R., Allen, L., Pipher, J., Hartmann, L., et al., 2004, *ApJ*, 154, 379.
- Nishiyama, S., et al., 2006, *ApJ*, 638, 839.
- Olmi, L., Testi L., 2002, *A&A*, 392, 1053-1068.
- Peterson, D., et al., submitted.
- Porras, A., et al., 2007, *ApJ*, 656, 493-504.
- Preibisch, T., 2003, *A&A*, 410, 951-959.
- Preibisch, T., 2004, *A&A*, 428, 569-577.
- Preibisch, T., Feigelson, E., 2005, *ApJS*, Vol. 160.
- Preibisch, T., Kim, , Favata, F., et al., 2005, *ApJS*, Vol. 160.

- Raymond, J. C., Smith, B. W., 1977, *ApJ*, 35, 419-439.
- Reach, W.T., et al., 2005, *ASP*, 117, 978-990.
- Rebull, L.M., et al., 2007, *astro-ph/0701711*.
- Rieke, G., et al., 2004, *ApJS*, 154, 25-29.
- Rieke, G.H., Lebofsky, M.J., 1985, *ApJ*, 288, 618-621.
- Romanov, M.M., et al., 2004, *ApJ*, 616, L151.
- Shu, F. 1992, *The Physics of Astrophysics*, Vol. II.
- Skrutskie, M.F., Cutri R.M., Stiening R., et al., 2006, *AJ*, 131, 1163.
- Slesnick, C. L., Hillenbrand, L. A., Carpenter, J. M., 2004, *ApJ*, 610, 1045-1063.
- Stern, D., Eisenhardt, P., Gorjian, V., et al., 2005, *ApJ*, 631, 163-168.
- Straižys, V., Černis, K., Bartasiūtė, S., 2003, *A&A*, 405, 585.
- Teixeira, P., Lada, C.J., Young E.T., Marengo M., Muench A., et al., 2006, *ApJ*, 636, L45-L48.
- Testi, L., Sargent, A., 1998, *ApJ*, 508, L91-L94.
- Testi, L., Sargent, A., Olmi L., Onella J., 2000, *ApJ*, 540, L53-L56.
- Young, M. H., et al., 2003, *A&A*, 408, 581-599.
- Werner, M.W., et al., 2004, *ApJS*, 154, 1.
- Whitney, B. A., Wood, K., Bjorkman, J. E., Wolff, M. J., 2003, *ApJ*, 591, 1049-1063.
- Whitney, B. A., Wood, K., Bjorkman, J. E., Cohen, M., 2003, *ApJ*, 598, 1079-1099.
- Whittet, D.C.B., 2003, *IOP, Dust in the Galactic Environment*, 2nd Ed..
- Williams, J., Meyers P., 1999, *ApJ* 518, L37-L40.
- Williams, J., Meyers P., 2000, *ApJ*, 537, 891-903.
- Wolk, S. J., Spitzbart, B. D., Bourke, T. L., Alves, J., 2006, *AJ*, 132, 1100-1125.
- Wolk, S. J., Bourke, T. L., et al., 2007, in prep.

Young, E.T., Teixeira, P.S., et al. , 2006, ApJ, 642, 972-978.

Table 1. Table of Source Identification Details

	IR-excess	X-ray Detected	Extremely Red	Total
Identified	200	67	3	229
Contam.	87	7	1	91
YSOs	113	60	2	138

Table 2. Table of Source Classifications

Class	IR-field	IRX-field	X-ray Detections
0/I	22	22	9 (43%)
Flat	16	15	8 (53%)
II	62	44	20 (46%)
Trans.	17	8	2 (25%)
III	21	21	21

Table 3. Table of class distribution comparison: Kolmogorov-Smirnov probabilities.

	I	Flat	II	Trans.	III
Random	2×10^{-7}	0.05	0.13	0.67	0.21
I	...	5.7×10^{-4}	1.2×10^{-5}	4.6×10^{-5}	3.0×10^{-5}
Flat	5.7×10^{-4}	...	0.45	0.28	0.73
II	1.2×10^{-5}	0.45	...	0.016	0.60
Trans.	4.6×10^{-5}	0.28	0.016	...	0.35

Table 4. Table of Coordinates & Other Identifiers

<i>Spitzer</i> ID	RA (2000)	Dec (2000)	EC ^a	Kaas ^b	Class 0 ^c	<i>Chandra</i> ID	GFG ID ^d
1	18:30:02.09	1:13:58.81	CK7
2	18:29:57.83	1:12:51.62	EC95	Kaas317/345	...	72	53
3	18:29:59.57	1:11:58.80	...	Kaas330	...	25	60
4	18:29:58.76	1:14:26.47	EC103	Kaas326	...	23	...
5	18:29:47.01	1:16:26.82	EC27	Kaas237
6	18:29:49.24	1:16:31.74	...	Kaas249
7	18:29:49.58	1:17:05.92	EC76	Kaas254	S68Nb	17	28
8	18:29:57.59	1:13:00.44	SVS4-10	Kaas312	...	12	46
9	18:29:56.88	1:14:46.62	CK3	Kaas307	...	67	43
10	18:30:02.73	1:12:28.14	EC129	Kaas347	PS2
11	18:29:49.11	1:16:19.97	SN68d
12	18:29:57.64	1:13:04.54
17	18:30:00.68	1:13:01.23
18	18:29:59.92	1:13:11.58	...	Kaas331
19	18:29:59.61	1:14:12.33	78	61
20	18:29:52.85	1:14:56.08	...	Kaas276	33
21	18:29:52.20	1:15:47.59	...	Kaas270	SMM10
22	18:29:52.20	1:15:59.02	20	32
23	18:29:48.09	1:16:44.98	...	Kaas241	SMM9/S68N
24	18:29:51.14	1:16:40.49	...	Kaas265	SMM5	18	30
27	18:29:58.18	1:15:21.91	CK4	Kaas321	...	74	55
28	18:30:00.20	1:14:03.56	79	62
30	18:30:01.09	1:13:24.44	EC121	Kaas341	...	81	66
31	18:30:01.53	1:15:14.93	EC123	...	SMM8
32	18:29:18.85	1:14:16.94
33	18:30:23.43	1:05:04.84
34	18:29:53.84	1:12:47.40
35	18:29:57.72	1:14:06.06	SVS20	Kaas314	SMM6	70	48
36	18:29:31.97	1:18:42.66	...	Kaas159	...	9	9
37	18:29:57.82	1:12:37.97	EC94	Kaas318	...	22	52
38	18:29:55.68	1:14:31.34	CK9	Kaas298	...	63	37
39	18:29:54.07	1:07:11.10	...	Kaas287
40	18:30:18.17	1:14:16.89	44	83
44	18:29:59.38	1:10:40.92
45	18:29:59.02	1:12:24.92	...	Kaas327
47	18:30:02.48	1:12:43.44
48	18:29:49.70	1:14:56.71	EC40	Kaas253
53	18:29:14.32	1:07:30.14
54	18:30:05.01	1:12:35.99
55	18:30:22.83	1:16:21.34
56	18:29:55.56	1:08:34.34
57	18:29:21.08	1:24:06.66
58	18:30:22.74	1:13:23.58
59	18:29:59.22	1:14:07.82	CK8	Kaas328	...	77	59
60	18:30:04.09	1:06:55.86
61	18:29:56.66	1:12:39.17	EC80	Kaas306	...	21	42

Table 4—Continued

<i>Spitzer</i> ID	RA (2000)	Dec (2000)	EC ^a	Kaas ^b	Class 0 ^c	<i>Chandra</i> ID	GFG ID ^d
62	18:29:55.19	1:13:22.43	EC73	Kaas294
64	18:29:38.18	1:09:17.53
65	18:29:43.92	1:07:20.99	...	Kaas219
66	18:29:51.43	1:09:32.94
67	18:30:09.22	1:17:52.66
68	18:29:47.19	1:07:16.02
69	18:29:53.83	1:13:30.80	EC68	Kaas285
70	18:29:57.81	1:12:28.17	EC91	Kaas320
71	18:29:44.28	1:04:53.50	...	Kaas221
72	18:29:04.26	1:18:39.08
73	18:30:07.70	1:12:04.49	...	Kaas366	...	86	75
74	18:30:13.28	1:02:48.93
75	18:29:32.24	1:12:39.94
76	18:30:16.97	1:13:07.47
77	18:30:00.89	1:22:03.59
78	18:30:03.41	1:16:19.45	EC135	Kaas348	...	84	69
79	18:29:46.28	1:10:25.33
80	18:29:56.53	1:12:59.53	SVS4-2	Kaas304	...	66	40
81	18:29:53.59	1:17:01.91	EC67	Kaas283	...	60	34
82	18:29:33.37	1:08:24.42	...	Kaas173
83	18:29:57.80	1:15:31.89	CK13	Kaas319	...	71	50
84	18:30:06.08	1:06:17.11	...	Kaas357	...	42	73
85	18:29:56.94	1:12:47.88	EC84	Kaas309	...	68	44
86	18:29:53.16	1:12:27.78
87	18:29:54.50	1:14:47.11	EC70	Kaas291	...	61	35
88	18:30:41.16	1:13:15.94
89	18:30:14.42	1:04:06.44
90	18:30:44.52	1:23:30.19
91	18:29:35.18	1:13:10.95
92	18:30:01.66	1:04:42.96
93	18:29:42.15	1:20:20.93	...	Kaas216	...	47	...
94	18:29:39.87	1:17:56.02	...	Kaas202	...	57	18
95	18:29:51.18	1:13:19.71	EC51	Kaas266	...	49	31
96	18:29:53.09	1:06:17.85
97	18:29:05.82	1:13:22.94
98	18:30:04.89	1:14:39.48	85	71
99	18:29:53.54	1:13:05.34
100	18:29:44.53	1:13:11.59	EC11	Kaas224	...	59	23
101	18:30:11.09	1:12:37.93	...	Kaas393	...	87	79
102	18:30:27.67	1:22:35.02
103	18:29:41.44	1:07:38.15	...	Kaas207
104	18:29:20.41	1:21:03.78
105	18:29:57.89	1:12:46.42	EC98	Kaas322	...	73	54
106	18:29:48.77	1:13:42.12	EC33	Kaas242
109	18:30:02.31	1:08:08.82
110	18:30:00.31	1:09:44.59	13	63

Table 4—Continued

<i>Spitzer</i> ID	RA (2000)	Dec (2000)	EC ^a	Kaas ^b	Class 0 ^c	<i>Chandra</i> ID	GFG ID ^d
112	18:29:56.28	1:13:21.14
114	18:29:49.69	1:15:28.85	...	Kaas258
115	18:29:38.59	1:18:01.39
118	18:30:01.79	1:18:59.84
119	18:29:29.80	1:21:57.38	5	6
122	18:29:13.01	1:07:00.64
124	18:29:08.17	1:05:44.68
127	18:29:37.67	1:11:30.01
128	18:30:23.12	1:20:09.65	46	85
134	18:29:37.58	1:11:17.55
136	18:29:16.36	1:08:22.13
140	18:30:37.33	1:16:09.02
143	18:30:53.70	1:11:20.64
156	18:30:00.07	1:03:05.81
157	18:30:22.39	1:20:44.12	45	84
158	18:30:00.60	1:15:20.21
161	18:30:17.29	1:21:32.83
165	18:29:58.43	1:12:50.35	75	...
166	18:30:13.96	1:08:51.47	...	Kaas407
170	18:30:09.43	1:02:47.06	...	Kaas379
174	18:30:03.58	1:16:41.04
176	18:29:41.52	1:10:04.52
180	18:29:47.64	1:04:22.28
181	18:30:19.60	1:05:34.31
187	18:30:16.80	1:19:17.13
189	18:30:03.01	1:19:49.71	83	...
190	18:29:57.39	1:14:50.47	88	45
192	18:29:57.65	1:10:53.56	69	47
193	18:29:57.55	1:10:47.01	50	...
195	18:30:01.24	1:15:03.73	82	67
196	18:29:59.11	1:11:20.09	76	58
198	18:29:59.05	1:11:13.82	24	57
199	18:29:47.21	1:22:34.69	40	27
201	18:29:55.34	1:10:34.31	62	36
203	18:30:05.50	1:14:24.87	51	72
204	18:29:56.33	1:12:18.04	65	39
205	18:29:56.17	1:10:57.66	64	38
209	18:29:50.53	1:08:58.22	41	29
215	18:29:42.32	1:12:01.99	58	21
216	18:30:00.64	1:13:40.38	Serpens13	Kaas338	...	80	65
218	18:29:49.47	1:12:04.29	48	...
220	18:30:24.44	1:19:50.66	36	...
221	18:29:22.70	1:10:33.09	37	2
224	18:29:31.64	1:15:05.59	54	...
225	18:29:33.06	1:17:16.68	56	11

^aIdentifiers from Eiroa et al. (1992).

^bIdentifiers from Kaas et al. (2004).

^cIdentifiers from Testi et al. (1998); Williams & Meyers (1999); Davis et al. (1999).

^dIdentifiers from Giardino et al. (2006).

Table 5. Table of Young Stellar Objects in Serpens

ID	J	H	K	$3.6\mu\text{m}$	$4.5\mu\text{m}$	$5.8\mu\text{m}$	$8.0\mu\text{m}$	$24.0\mu\text{m}$	Class	CID ^a	α_{IRAC} ^b	A_K ^c
1	>16.044	14.921±0.118	13.389±0.046	10.651±0.003	9.806±0.002	9.081±0.003	8.207±0.002	4.030±0.004	0/1	...	-0.06	...
2	15.752±0.093	12.455±0.045	10.518±0.029	8.646±0.004	7.680±0.003	6.874±0.004	5.639±0.004	1.099±0.013	0/1	72	0.56	...
3	>17.913	>17.371	14.649±0.099	8.959±0.003	7.263±0.002	6.195±0.002	5.309±0.001	1.504±0.006	0/1	25	1.27	...
4	>15.185	14.025±0.069	11.843±0.042	9.485±0.004	8.383±0.005	7.332±0.005	6.619±0.005	2.471±0.021	0/1	23	0.46	...
5	>17.731	>15.836	13.403±0.041	11.041±0.004	10.218±0.005	9.614±0.007	8.910±0.004	5.463±0.022	0/1	...	-0.44	...
6	>18.248	>17.326	13.446±0.04	10.742±0.004	9.322±0.004	8.255±0.003	7.051±0.006	1.665±0.022	0/1	...	1.35	...
7	>16.889	15.658±0.145	12.67±0.036	9.621±0.002	8.282±0.003	7.302±0.002	6.447±0.002	2.741±0.009	0/1	17	0.76	...
8	>16.454	>14.104	13.055±0.085	9.188±0.007	7.665±0.004	6.747±0.004	5.977±0.007	1.431±0.014	0/1	12	0.77	...
9	12.046±0.045	10.785±0.057	9.298±0.034	6.822±0.002	6.079±0.002	5.541±0.001	4.228±0.001	0.574±0.008	0/1	67	0.06	...
10	15.204±0.061	11.92±0.033	9.917±0.023	7.716±0.002	6.789±0.002	6.044±0.002	5.199±0.001	1.267±0.004	0/1	...	0.01	...
11	>18.253	>17.301	14.925±0.200	11.032±0.005	8.656±0.004	6.897±0.004	5.178±0.002	-0.03±0.1 ^c	0/1	...	2.21	...
12	16.046±0.113	13.765±0.055	12.023±0.052	10.137±0.008	9.217±0.006	0/1	...	0.74	...
17	14.129±0.059	12.460±0.029	11.462±0.029	10.354±0.023	...	0/1	...	1.39	...
18	12.629±0.019	9.513±0.003	7.672±0.002	6.262±0.002	0.987±0.008	0/1	...	4.35	...
19	12.341±0.035	11.406±0.031	10.313±0.044	...	5.242±0.037	0/1	78	1.03	...
20	11.386±0.005	9.433±0.003	8.114±0.002	6.979±0.003	1.876±0.006	0/1	...	2.16	...
21	11.534±0.005	9.617±0.003	8.724±0.003	7.958±0.002	1.729±0.009	0/1	...	1.12	...
22	15.781±0.081	12.697±0.012	11.027±0.009	10.235±0.012	...	0/1	20	3.40	...
23	12.969±0.006	11.118±0.004	10.039±0.005	9.069±0.005	3.507±0.036	0/1	...	1.54	...
24	10.011±0.002	8.701±0.005	7.404±0.002	6.356±0.002	1.813±0.007	0/1	18	1.38	...
27	13.072±0.029	11.188±0.028	9.859±0.022	8.278±0.002	7.654±0.002	7.181±0.002	6.405±0.001	2.774±0.011	FS	74	-0.74	...
28	15.706±0.086	13.912±0.033	12.821±0.018	11.320±0.006	10.749±0.004	10.094±0.024	9.061±0.021	5.577±0.034	FS	79	-0.26	...
30	>17.925	15.367±0.12	13.22±0.033	11.117±0.003	10.314±0.003	9.862±0.006	9.244±0.006	4.9099±0.103	FS	81	-0.77	...
31	11.544±0.083	6.321±0.050	0/1
32	16.674±0.16	15.453±0.135	14.848±0.148	13.720±0.013	12.349±0.011	11.467±0.017	10.898±0.024	7.527±0.022	FS	...	0.34	...
33	13.403±0.03	12.434±0.035	11.779±0.023	10.845±0.002	10.287±0.002	9.892±0.005	9.113±0.003	5.268±0.005	FS	...	-0.91	...
34	>18.32	>17.294	15.115±0.166	14.053±0.010	13.536±0.012	13.013±0.031	12.136±0.029	8.954±0.061	FS	...	-0.67	...
35	12.222±0.026	9.242±0.036	7.051±0.024	5.231±0.002 ^d	4.386±0.002 ^d	3.426±0.001	2.591±0.001 ^d	-0.33±0.1 ^c	FS	70	0.21	...
36	11.631±0.024	9.803±0.032	8.584±0.021	6.968±0.001	5.921±0.002	5.045±0.001	3.917±0.001	0.51±0.1 ^c	FS	9	0.62	...
37	>17.197	14.412±0.061	11.664±0.028	9.709±0.003	8.793±0.004	8.226±0.005	7.568±0.005	...	FS	22	-0.45	...
38	15.337±0.05	12.469±0.026	10.653±0.018	9.281±0.003	8.268±0.002	7.442±0.002	6.732±0.003	3.708±0.016	FS	63	0.06	...
39	15.981±0.118	14.356±0.049	13.51±0.047	11.808±0.004	11.358±0.004	10.964±0.008	10.226±0.009	7.057±0.007	FS	...	-1.07	...
40	13.307±0.026	11.773±0.032	10.895±0.02	10.476±0.002	9.931±0.002	9.278±0.003	8.275±0.004	4.393±0.007	FS	44	-0.32	...
44	14.139±0.010	12.052±0.005	10.931±0.007	10.182±0.007	6.824±0.014	FS	...	1.59	...
45	12.774±0.007	11.801±0.006	11.067±0.012	10.176±0.011	5.899±0.012	FS	...	0.09	...

48

Table 5—Continued

ID	J	H	K	3.6 μ m	4.5 μ m	5.8 μ m	8.0 μ m	24.0 μ m	Class	CID ^a	α_{IRAC} ^b	A_K ^c
47	13.543±0.011	12.669±0.013	11.707±0.046	11.153±0.063	...	FS	...	-0.06	...
48	10.788±0.003	9.193±0.003	8.171±0.002	7.393±0.002	4.225±0.020	FS	...	0.99	...
53	14.609±0.036	13.658±0.037	13.147±0.032	12.478±0.005	12.162±0.005	11.918±0.015	11.329±0.013	8.718±0.041	2	...	-1.58	0.21
54	15.949±0.11	14.696±0.096	13.732±0.051	12.701±0.005	12.276±0.003	11.865±0.019	11.224±0.025	...	2	...	-1.18	0.28
55	15.619±0.084	14.426±0.068	13.589±0.057	13.013±0.012	12.748±0.030	12.477±0.057	2	...	-1.85	0.29
56	>14.229	14.768±0.098	14.319±0.107	13.248±0.014	12.755±0.011	2	...	-0.93	...
57	16.277±0.132	15.353±0.114	14.764±0.115	...	13.947±0.031	2	0.09
58	16.021±0.094	15.035±0.111	14.547±0.091	13.733±0.017	13.311±0.015	12.592±0.168	2	...	-0.67	0.29
59	11.75±0.025	10.368±0.03	9.505±0.02	8.103±0.003	7.448±0.004	6.888±0.009	6.153±0.009	4.030±0.015	2	77	-0.64	0.57
60	16.773±0.203	14.876±0.077	14.168±0.067	13.358±0.008	13.066±0.009	12.660±0.023	12.112±0.038	8.201±0.016	2	...	-1.43	0.45
61	>18.127	>16.539	14.056±0.056	10.683±0.004	9.269±0.004	8.761±0.005	8.428±0.005	5.501±0.025	2	21	-0.39	...
62	16.035±0.108	13.469±0.036	12.027±0.025	10.830±0.004	10.266±0.004	9.893±0.006	9.076±0.004	4.927±0.008	2	...	-0.90	1.92
64	15.903±0.106	14.751±0.073	14.515±0.116	13.069±0.022	13.069±0.023	2	...	-2.86 ^e	0.58
65	13.896±0.028	12.45±0.031	11.596±0.024	10.509±0.002	10.065±0.002	9.737±0.004	9.329±0.004	6.961±0.009	2	...	-1.53	0.68
66	15.666±0.073	14.963±0.092	>13.202	13.692±0.014	13.402±0.017	12.897±0.043	12.697±0.071	...	2	...	-1.68	...
67	15.419±0.065	13.974±0.046	12.953±0.032	11.363±0.003	10.878±0.003	10.503±0.006	9.948±0.005	7.107±0.012	2	...	-1.27	0.53
68	15.912±0.09	14.818±0.068	14.427±0.086	13.815±0.009	13.386±0.009	13.086±0.038	12.168±0.027	...	2	...	-1.03	0.52
69	16.453±0.146	14.286±0.048	13.01±0.035	11.897±0.005	11.531±0.005	10.889±0.009	10.269±0.011	7.266±0.036	2	...	-0.94	1.44
70	>18.165	15.823±0.176	12.969±0.033	10.856±0.004	9.908±0.003	9.466±0.011	8.967±0.014	6.045±0.023	2	...	-0.77	3.51
71	8.518±0.019	6.548±0.038	5.382±0.02	...	4.267±0.002	3.448±0.001	...	-0.241±0.009	2	...	0.18	1.23
72	16.676±0.185	15.988±0.192	15.489±0.216	14.466±0.019	14.370±0.025	2	3	-2.49 ^e	...
73	12.248±0.023	10.838±0.032	10.068±0.023	8.944±0.003	8.475±0.003	8.072±0.002	7.301±0.001	4.336±0.003	2	86	-1.01	0.70
74	13.719±0.029	12.769±0.033	12.351±0.025	11.836±0.004	11.635±0.004	11.420±0.012	10.786±0.017	7.582±0.023	2	...	-1.69	0.29
75	16.296±0.113	15.726±0.156	14.856±0.122	14.658±0.0168	14.579±0.022	14.266±0.079	2	...	-2.13 ^e	...
76	16.479±0.147	15.176±0.137	14.241±0.086	13.374±0.009	12.927±0.007	12.606±0.022	12.017±0.033	8.314±0.058	2	...	-1.34	0.38
77	15.86±0.093	15.084±0.11	14.515±0.10	13.965±0.026	13.792±0.028	13.361±0.127	2	...	-1.72	...
78	12.283±0.03	11.053±0.035	10.382±0.026	9.709±0.002	9.317±0.002	8.949±0.003	7.749±0.002	4.485±0.004	2	84	-0.65	0.51
79	13.210 ±0.026	12.309±0.028	11.918±0.023	11.245±0.002	10.923±0.003	10.594±0.006	10.038±0.005	7.848±0.008	2	...	-1.49	0.23
80	15.013±0.056	12.805±0.035	11.522±0.025	10.196±0.004	9.637±0.005	9.088±0.007	8.412±0.008	5.136±0.037	2	66	-0.82	1.48
81	12.605±0.022	11.239±0.031	10.411±0.021	9.577±0.002	9.248±0.002	8.923±0.003	8.324±0.002	5.927±0.013	2	60	-1.45	0.58
82	9.793±0.026	9.369±0.027	9.211±0.023	8.841±0.003	8.521±0.004	8.001±0.002	6.821±0.003	4.097±0.004	2	...	-0.54	...
83	16.206±0.138	12.792±0.036	10.805±0.022	9.209±0.003	8.574±0.004	8.279±0.003	7.753±0.004	4.698±0.024	2	71	-1.26	2.76
84	12.94±0.026	11.833±0.032	11.23±0.022	10.499±0.002	10.125±0.002	9.775±0.004	8.903±0.003	5.791±0.003	2	42	-1.06	0.38
85	15.168±0.051	12.473±0.035	11.087±0.025	9.919±0.004	9.513±0.006	9.029±0.006	8.591±0.017	...	2	68	-1.32	2.17
86	16.834±0.002	15.682±0.141	14.453±0.094	13.527±0.008	13.119±0.008	12.642±0.021	11.777±0.017	...	2	...	-0.86	1.33

Table 5—Continued

ID	J	H	K	3.6 μ m	4.5 μ m	5.8 μ m	8.0 μ m	24.0 μ m	Class	CID ^a	α_{IRAC} ^b	A_K ^c
87	14.174±0.041	13.332±0.042	12.8 ±0.035	12.300±0.008	12.132±0.009	11.937±0.028	11.847±0.053	...	3	61	-2.35	0.02
88	14.504±0.038	13.728±0.045	13.244±0.034	12.495±0.005	12.109±0.005	11.645±0.012	10.886±0.013	7.726±0.048	2	...	-1.02	...
89	15.246±0.065	14.312±0.056	13.921±0.065	12.962±0.007	12.484±0.006	12.074±0.017	11.377±0.015	8.868±0.016	2	...	-1.07	0.29
90	>14.481	14.69±0.083	14.501±0.092	13.888±0.016	13.516±0.013	2	...	-1.41	...
91	15.484±0.07	14.451±0.08	13.69±0.068	12.873±0.006	12.579±0.006	12.242±0.017	11.783±0.016	...	2	...	-1.62	0.11
92	16.069±0.115	14.187±0.052	13.097±0.034	12.047±0.005	11.433±0.004	11.062±0.009	10.198±0.014	6.847±0.025	2	...	-0.80	1.16
93	13.286±0.027	12.517±0.035	12.042±0.03	11.522±0.005	11.195±0.003	10.647±0.006	9.338±0.003	6.351±0.003	2	47	-0.35	...
94	14.471±0.034	12.83±0.032	11.937±0.026	10.983±0.003	10.573±0.003	10.198±0.006	9.388±0.005	6.294±0.006	2	57	-1.06	0.95
95	16.482±0.141	14.512±0.056	13.601±0.047	12.759±0.006	12.438±0.007	12.129±0.019	11.445±0.021	8.558±0.022	2	49	-1.38	1.44
96	14.383±0.035	13.052±0.032	12.561±0.028	11.429±0.003	11.276±0.003	10.913±0.007	10.236±0.006	7.493±0.011	2	...	-1.48	0.77
97	16.341±0.129	15.796±0.154	>14.814	14.482±0.015	14.382±0.022	2	...	-2.47 ^e	...
98	13.663±0.029	12.716±0.032	12.241±0.026	11.734±0.004	11.281±0.004	10.909±0.008	10.260±0.008	8.116±0.025	2	85	-1.20	0.24
99	14.89±0.041	14.127±0.036	13.742±0.057	13.013±0.008	12.708±0.008	12.518±0.022	12.105±0.027	...	2	...	-1.86	0.03
100	13.229±0.024	12.217±0.035	11.765±0.028	11.262±0.003	11.033±0.003	10.669±0.007	9.837±0.006	6.962±0.004	2	59	-0.23	0.36
101	>13.258	12.481±0.037	11.956±0.026	11.147±0.003	10.893±0.003	10.238±0.006	9.347±0.005	6.425±0.005	2	87	-0.74	0.14
102	15.948±0.119	15.315±0.129	14.482±0.093	14.212±0.017	14.161±0.018	13.819±0.089	2	...	-2.12 ^e	...
103	11.603±0.022	10.386±0.028	9.644±0.019	8.728±0.002	8.399±0.002	8.073±0.002	7.244±0.001	4.169±0.005	2	...	-1.18	0.42
104	12.833±0.033	11.250±0.041	10.325±0.028	9.449±0.002	9.149±0.002	8.899±0.003	8.517±0.003	5.984±0.013	2	...	-1.82	0.83
105	>16.553	12.520±0.042	9.969±0.034	8.449±0.003	7.714±0.003	7.053±0.004	6.353±0.006	...	2	73	-0.46	3.45
106	>17.230	15.288±0.106	13.451±0.041	12.075±0.004	11.368±0.003	10.954±0.008	10.309±0.008	7.491±0.015	2	...	-0.89	1.84
109	13.247±0.006	12.152±0.005	11.381±0.011	10.677±0.015	8.678±0.033	2	...	0.06	...
110	10.505±0.002	8.989±0.003	7.971±0.002	7.236±0.002	4.817±0.003	2	13	0.86	...
112	14.965±0.131	13.780±0.068	13.038±0.111	12.531±0.091	...	2	...	-0.11	...
114	12.804±0.019	11.725±0.029	11.124±0.039	10.432±0.049	...	2	...	-0.21	...
115	14.643±0.018	14.281±0.025	14.123±0.071	13.668±0.157	...	2	...	-1.81	...
118	14.60±0.027	14.337±0.025	14.036±0.073	13.536±0.101	...	2	...	-1.65	...
119	14.209±0.016	13.627±0.050	13.021±0.045	...	2	5	-1.09	...
122	8.751±0.02	7.274±0.047	6.595±0.02	6.182±0.001	6.215±0.002	5.971±0.002	5.819±0.002	4.912±0.004	TD	...	-2.42	0.89
124	10.659±0.022	10.241±0.031	10.071±0.019	9.879±0.002	9.952±0.002	9.865±0.005	9.678±0.006	7.507±0.008	TD	...	-2.63	...
127	11.456±0.022	9.586±0.027	8.825±0.024	8.166±0.002	8.179±0.003	7.931±0.002	7.722±0.002	6.214±0.015	TD	...	-2.33	1.34
128	13.338±0.029	12.564±0.033	12.195±0.03	11.973±0.004	11.907±0.005	11.936±0.016	11.936±0.038	8.051±0.033	TD	46	-2.86	0.06
134	11.211±0.022	9.327±0.027	8.507±0.021	7.869±0.002	7.855±0.002	7.637±0.002	7.462±0.002	6.688±0.034	TD	...	-2.38	1.35
136	16.325±0.128	15.326±0.115	14.820±0.132	14.217±0.015	13.803±0.017	13.633±0.073	>12.029	8.536±0.036	2	...	-1.75	0.29
140	10.388±0.022	8.834±0.027	8.236±0.024	7.874±0.002	7.939±0.002	7.738±0.002	7.651±0.002	7.134±0.029	TD	...	-2.58	1.00
143	11.12±0.024	9.618±0.023	8.926±0.021	8.464±0.002	8.732±0.003	8.424±0.003	8.335±0.002	7.548±0.009	TD	...	-2.64	0.92

Table 5—Continued

ID	J	H	K	$3.6\mu\text{m}$	$4.5\mu\text{m}$	$5.8\mu\text{m}$	$8.0\mu\text{m}$	$24.0\mu\text{m}$	Class	CID ^a	α_{IRAC} ^b	A_K ^c
156	14.159±0.031	12.702±0.031	12.101±0.023	11.688±0.004	11.487±0.004	11.155±0.013	10.037±0.023	5.657±0.016	TD	...	-0.98	0.90
157	13.1 ±0.027	12.237±0.036	11.906±0.03	11.562±0.004	11.466±0.004	11.369±0.012	...	7.178±0.023	TD	45	-2.51	0.24
158	>17.663	12.635±0.035	8.987±0.022	6.771±0.001	6.369±0.002	5.849±0.001	5.793±0.001	5.181±0.012	TD	...	-1.71	6.26
161	9.747±0.021	8.19±0.049	7.542±0.024	7.141±0.002	7.089±0.002	6.897±0.003	6.694±0.003	5.464±0.004	TD	...	-2.35	1.01
165	>18.127	14.752±0.070	12.256±0.025	10.61±0.006	10.058±0.008	9.622±0.011	9.011±0.021	...	TD	75	-1.05	3.89
166	13.787±0.03	12.744±0.035	12.359±0.029	11.883±0.004	11.643±0.004	11.369±0.011	10.640±0.009	7.362±0.007	TD	...	-1.46	0.47
170	10.632±0.023	8.944±0.028	8.086±0.027	7.496±0.001	7.530±0.002	7.266±0.002	7.019±0.002	5.337±0.004	TD	...	-2.28	1.06
174	>18.198	>16.001	14.243±0.069	12.698±0.005	12.175±0.006	11.870±0.016	11.241±0.018	7.796±0.037	TD	...	-1.24	...
176	12.928±0.039	11.078±0.038	10.331±0.03	9.854±0.002	9.832±0.002	9.584±0.004	9.437±0.004	7.411±0.006	TD	...	-2.36	1.32
180	11.279±0.005	10.974±0.005	10.652±0.018	10.096±0.014	5.873±0.015	TD	...	-1.52	...
181	14.713±0.021	14.608±0.021	...	13.422±0.066	7.120±0.007	2	...	-1.73	...
187	16.182±0.121	15.754±0.170	15.207±0.157	14.943±0.033	14.913±0.039	3	35	-2.74	...
189	16.249±0.122	15.936±0.190	15.047±0.143	14.783±0.021	14.799±0.031	14.916±0.125	3	83	-3.14	...
190	13.299±0.031	11.669±0.03	10.942±0.026	10.237±0.007	10.067±0.011	9.713±0.037	3	88	-1.87	1.08
192	8.107±0.021	8.13 ±0.053	8.064±0.016	8.049±0.002	8.064±0.002	8.121±0.002	8.049±0.002	7.726±0.019	3	69	-2.91	...
193	9.149±0.021	9.141±0.039	9.072±0.023	...	9.057±0.003	9.088±0.004	9.012±0.004	...	3	50	-2.96	...
195	15.431±0.072	13.108±0.032	12.022±0.02	11.284±0.006	11.084±0.007	10.880±0.016	10.796±0.022	...	3	82	-2.31	1.81
196	14.206±0.036	12.557±0.031	11.877±0.026	11.406±0.003	11.253±0.004	11.221±0.009	11.122±0.019	...	3	76	-2.58	1.10
198	>16.917	>16.191	14.442±0.09	12.457±0.006	11.851±0.005	11.503±0.013	11.295±0.024	...	3	24	-1.57	...
199	11.797±0.022	10.52 ±0.031	10.082±0.021	9.819±0.002	9.792±0.002	9.765±0.005	9.651±0.005	...	3	40	-2.70	0.71
201	14.041±0.032	13.345±0.033	12.923±0.033	12.548±0.005	12.481±0.006	12.397±0.019	12.509±0.039	...	3	62	-2.83	...
203	15.156±0.052	14.424±0.056	14.104±0.069	13.734±0.009	13.563±0.012	13.449±0.062	13.382±0.083	...	3	51	-2.49	0.04
204	15.333±0.065	14.245±0.056	13.59 ±0.044	13.146±0.008	12.966±0.013	12.768±0.044	12.989±0.071	...	3	65	-2.68	0.29
205	12.496±0.025	11.705±0.028	11.412±0.023	11.392±0.004	11.304±0.004	11.331±0.010	11.100±0.012	...	3	64	-2.58	0.16
209	14.375±0.037	13.016±0.032	12.527±0.026	12.157±0.007	12.059±0.009	11.822±0.024	11.728±0.067	...	3	41	-2.36	0.79
215	>16.836	14.37 ±0.059	12.877±0.035	11.991±0.004	11.758±0.005	11.604±0.012	11.610±0.022	...	3	58	-2.45	2.35
216	13.359±0.032	11.162±0.032	10.117±0.022	9.587±0.002	9.395±0.002	9.260±0.005	9.247±0.005	...	3	80	-2.50	1.68
218	16.197±0.104	14.833±0.065	14.427±0.078	13.910±0.011	13.859±0.015	13.697±0.049	13.844±0.105	...	3	48	-2.78	0.80
220	12.446±0.024	11.945±0.028	11.825±0.023	11.762±0.003	11.811±0.005	11.705±0.019	3	36	-2.77	...
221	12.161±0.026	11.116±0.031	10.895±0.023	10.706±0.002	10.658±0.003	10.682±0.007	10.627±0.0081	...	3	37	-2.81	0.47
224	15.957±0.093	14.719±0.052	14.185±0.064	13.912±0.009	13.849±0.014	13.921±0.058	13.921±0.110490	...	3	54	-2.93	0.65
225	11.377±0.022	10.33 ±0.031	9.947±0.024	9.631±0.002	9.597±0.002	9.532±0.004	9.493±0.005	...	3	56	-2.72	0.47

^a *Chandra* X-ray Identifier number.^b Slope of SED calculated from available IRAC data points. Note slopes of FS objects fall between $-0.3 > \alpha > 0.3$ when $24\mu\text{m}$ point is included.

^cThis source was saturated at $24 \mu m$, the photometry was fit using the PSF wings as described in text.

^dPhotometry at this wavelength is saturated.

^eSlope & classification uncertain due to lack of photometry in all *Spitzer* bands. The IR-excess may be due to a mismatch between the 2MASS & IRAC photometry.

Table 6. Table of submm and mm sources

Identifier	RA ^a J2000	Dec ^a J2000	<i>Spit.</i> RA J2000	<i>Spit.</i> Dec J2000	3.6 μ m (mJy)	4.5 μ m (mJy)	5.8 μ m (mJy)	8.0 μ m (mJy)	24 μ m (mJy)	70 μ m (mJy)	450 μ m ^b (mJy)	850 μ m ^b (mJy)	3mm ^c (mJy)	3.5cm ^d (mJy)	CXO ^e I.D.
SMM1	18:29:49.69	1:15:20.55	18:29:49.66	1:15:21.56	10.7 ^f	1538	28034	35700	6100	233.	7.54	...
SMM2	18:30:00.33	1:12:55.33	3400	700
SMM3	18:29:59.41	1:14:01.25	18:29:59.27	1:14:02.90	472	...	7100	1500
SMM4	18:29:56.73	1:13:17.07	18:29:56.69	1:13:20.71	0.29 ^f	2.53 ^f	2.25 ^f	10800	2900	...	0.12	...
SMM5	18:29:51.16	1:16:40.65	18:29:51.14	1:16:40.47	27.8	59.4	125	183	1376	3705	3900	900	20.7	0.15	18
SMM6	18:29:57.71	1:14:08.12	18:29:57.73	1:14:06.03	2269	3163	4899	5897	9676	5452	1900	500	...	0.17	70
SMM8	18:30:01.79	1:15:09.43	18:30:01.53	1:15:14.90	1.55 ^g	21.6	...	1300	400
SMM9	18:29:48.16	1:16:44.43	18:29:48.10	1:16:44.97	1.82	6.41	11.1	15.1	289	5664	9100	1600	36.1	0.28	...
S68Nb	18:29:49.55	1:17:10.53	18:29:49.58	1:17:05.89	39.8	87.4	137	169	585	17.7	...	17
S68Nc	18:29:48.71	1:16:57.00	18:29:48.88	1:16:55.23	2.41 ^g	0.27 ^g	20.4
S68Nd	18:29:48.96	1:16:23.01	18:29:49.12	1:16:19.95	10.8	61.9	200	543	7340	7489	32.3
SMM10	18:29:52.08	1:15:48.74	18:29:52.20	1:15:47.59	6.83	25.5	37.2	42.1	1487	4953	2700	600	25.3	0.14	...
SMM11	18:29:59.67	1:11:32.27	[18:29:59.57]	[1:11:58.77]	2700	900	[3]
PS2 ^h	18:30:03.15	1:12:27.53	18:30:02.73	1:12:28.11	230	345	439	534	2275	2319

^aCoordinates from Testi et al. (1998), except S68Nb-d taken from Williams & Meyers (2000). Brackets indicate possible offset location of SMM11.

^bPeak Fluxes in mJy/beam from Davis et al. (1999), assuming all flux from source falls in one beam.

^cCoordinates & Peak Fluxes from Williams & Meyers (2000).

^dPeak Fluxes from Eiroa et al. (2005).

^eThe *Chandra* Identifier number, as in Table 4.

^fExtended nebulous source.

^g*Spitzer* fluxes associated with sources contaminated by flux from nearby bright objects.

^hDetected in Testi et al. (1998), no flux listed.

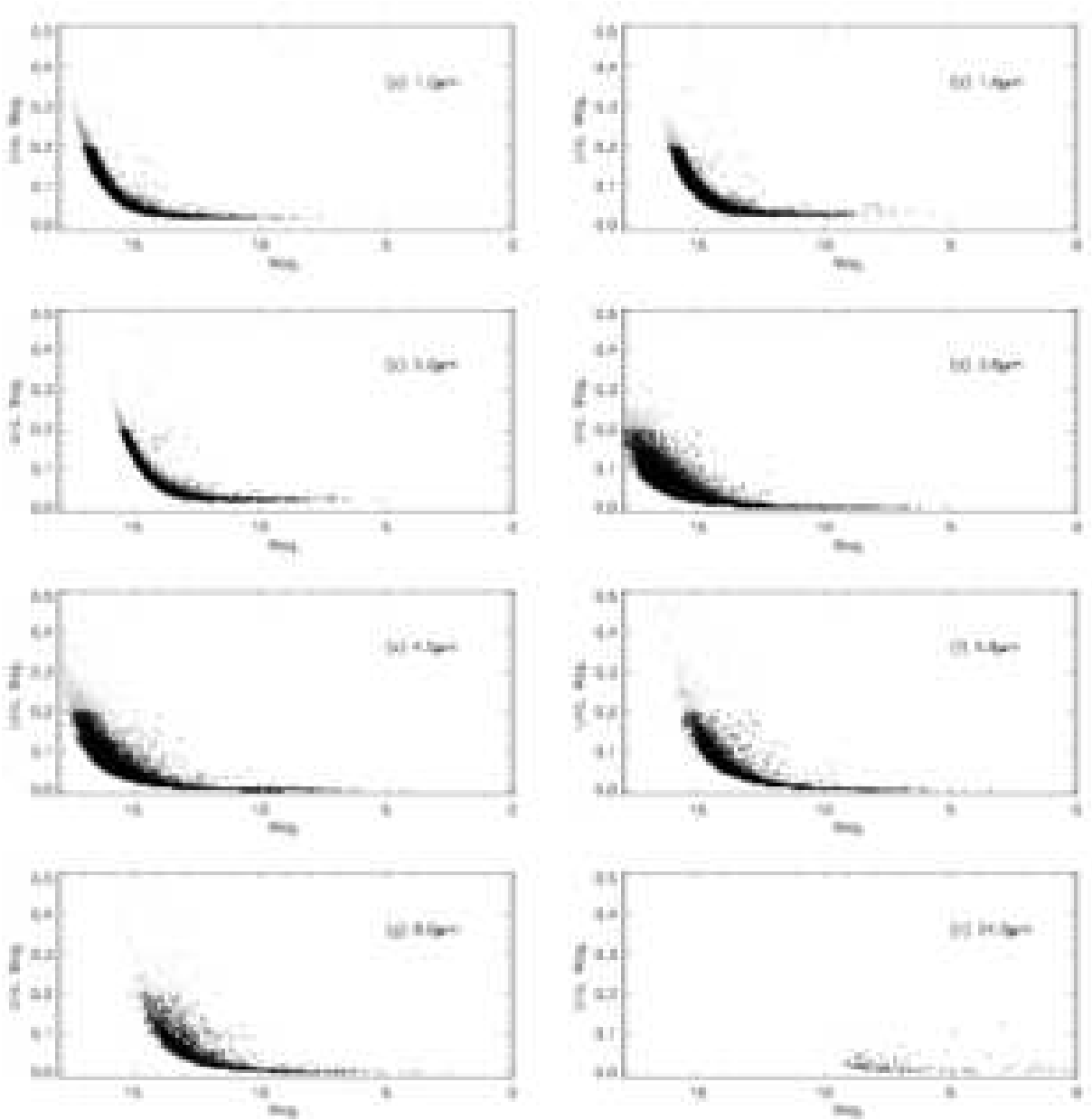


Fig. 1.— The magnitude vs magnitude uncertainty for each of the eight IR bands used in the study. The black points indicate those sources having errors in magnitude less than 0.2 mag, the grey points those with larger errors. This cutoff was applied to all selection techniques. (a) J , (b) H , (c) K_s , (d) $3.6 \mu m$, (e) $4.5 \mu m$, (f) $5.8 \mu m$, (g) $8.0 \mu m$, (h) $24 \mu m$. The near-IR data is from the 2MASS catalogue.

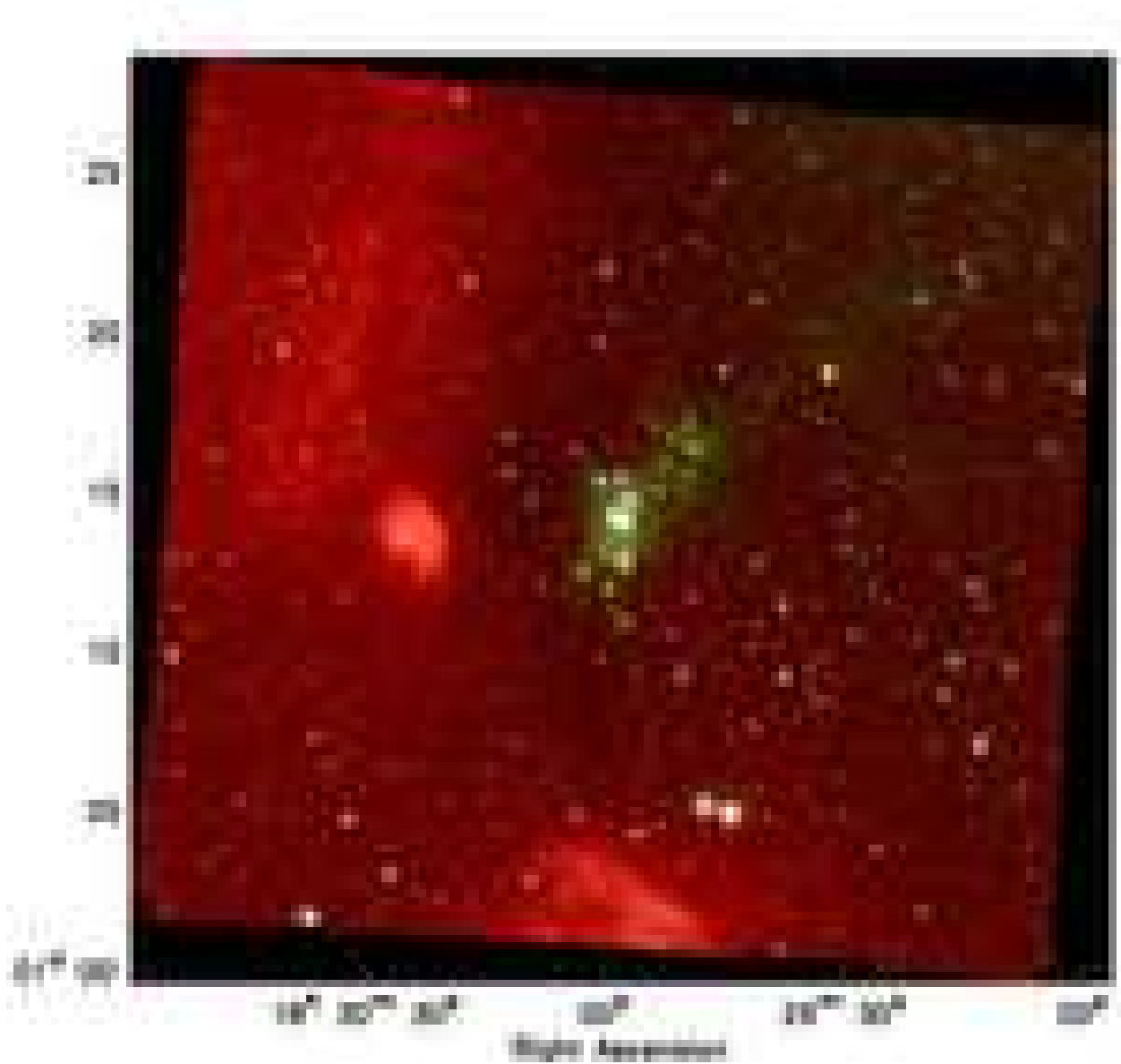


Fig. 2.— The Serpens cloud core region. A three band false color image of Serpens using IRAC on *Spitzer*. Blue is $3.6 \mu m$, Green is $4.5 \mu m$, and Red is $8.0 \mu m$. Much of the reddish hue in the image is due to the diffuse PAH emission. Emission from shocked hydrogen is visible in green. The light blue-green is scattered light.

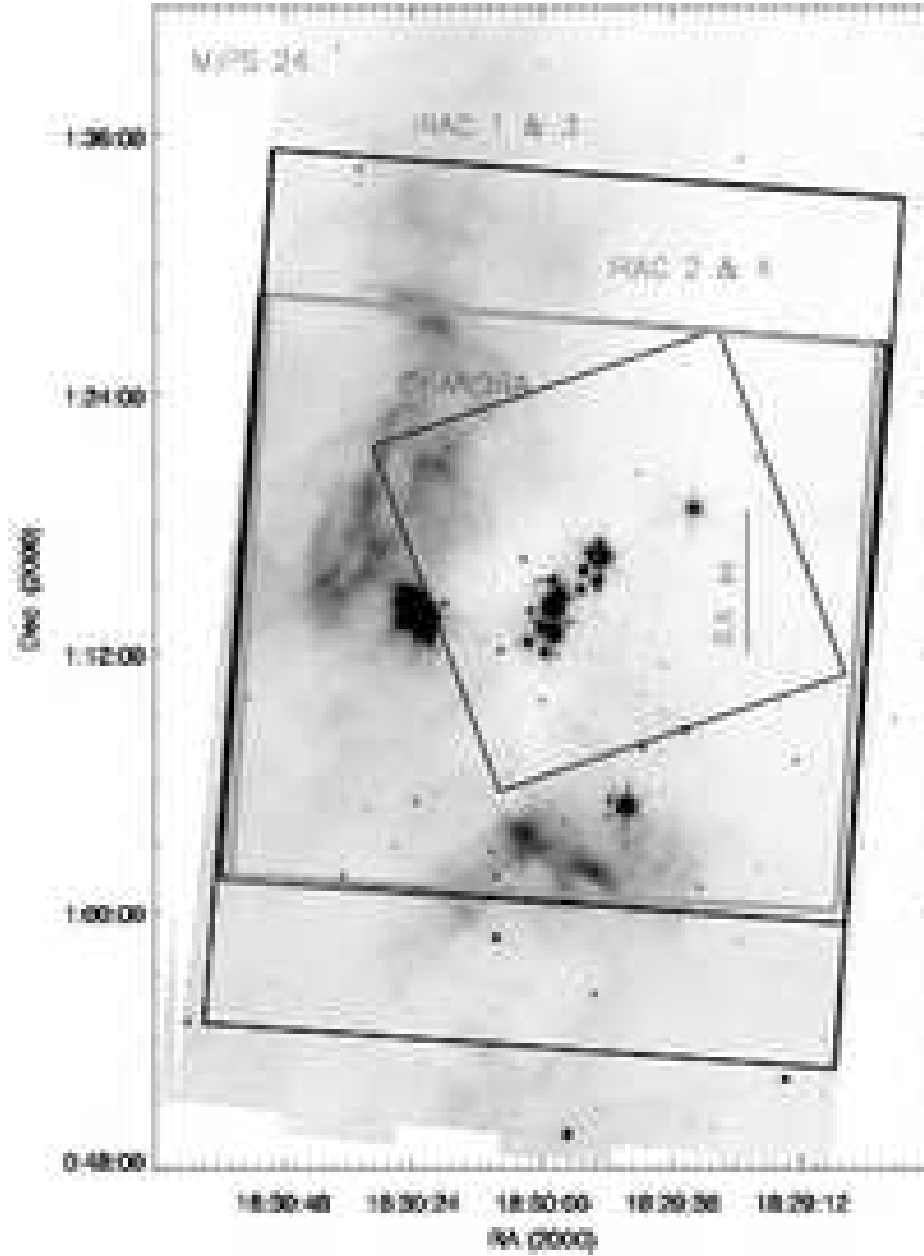


Fig. 3.— A grey-scale image of the Serpens cloud core at $24 \mu m$ showing the entire field of view. Overlaid, in black, are the outlines of the fields of view of the IRAC $3.6 \text{ \& } 5.8 \mu m$ (Chs. 1 & 3) and $4.5 \text{ \& } 8.0 \mu m$ (Chs. 2 & 4), and the *Chandra* field of view (the IRX-field). The IR-field, which contains complete coverage in all the infrared bands, is outlined in gray.

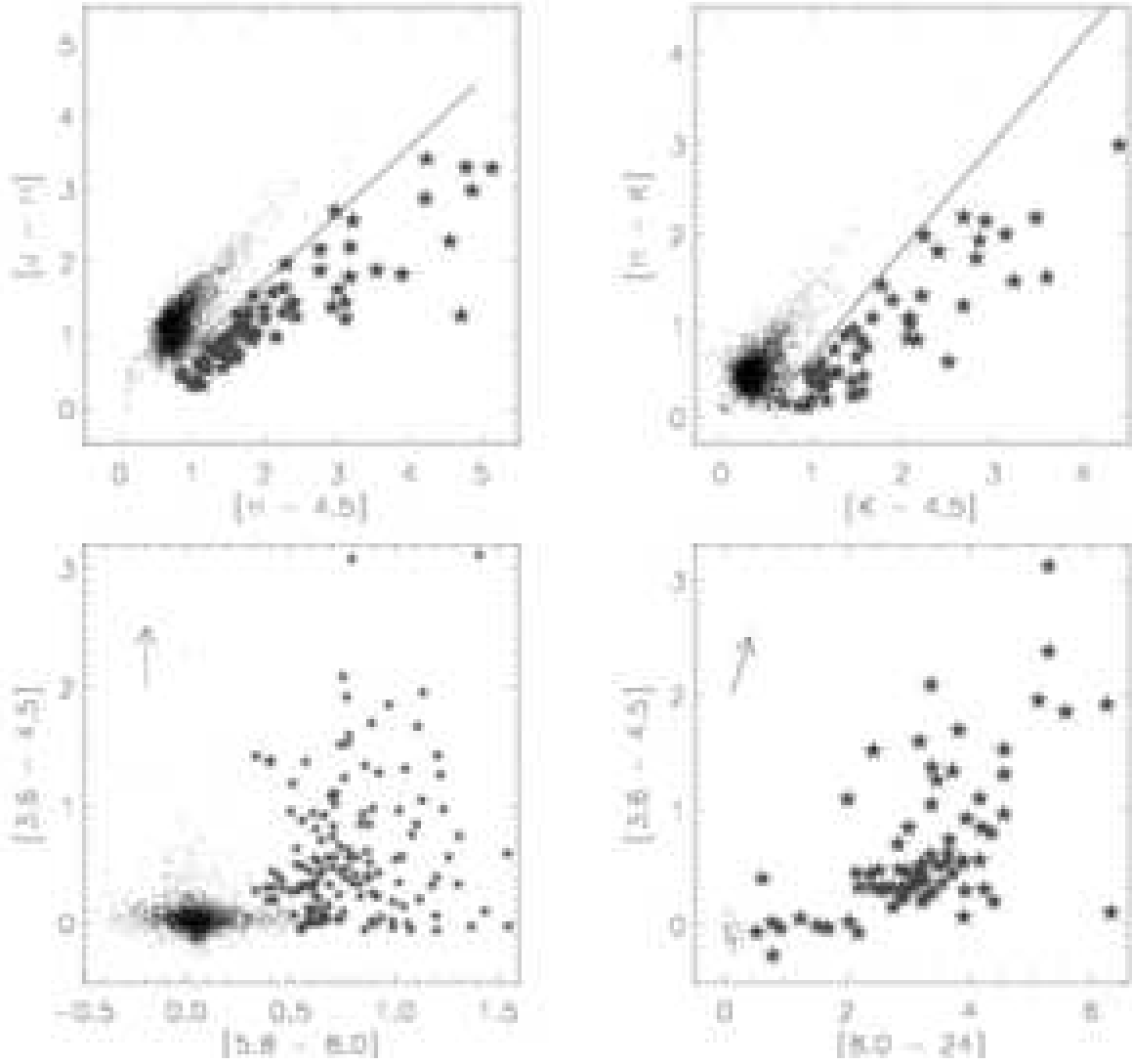


Fig. 4.— The four color-color diagrams used to identify young stellar objects. *Top Left*: the $J-H$ vs. $H-[4.5]$ diagram. The solid line shows the reddening vector for these wavelengths, objects with $H-[4.5]$ greater than one sigma below the reddening vector are considered to have an excess. The black dots indicate those objects classified as having no excess in this diagram, the grey stars indicate those sources with an excess. *Top Right*: The $H-K$ vs. $K-[4.5]$ diagram. Similar to above, with stars indicating those sources with excess in their $K-[4.5]$ colors. *Bottom Left*: The IRAC four color-color diagram, $[3.6]-[4.5]$ vs. $[5.8]-[8.0]$. The locus for field stars lies on the origin, the spread in the $[5.8]-[8.0]$ colors is in part due contamination from nebulosity and from contamination from star-forming galaxies with strong PAH emission in the 5.8 and $8.0 \mu\text{m}$ bands. *Bottom Right*: A MIPS and IRAC color-color diagram: $[3.6]-[4.5]$ vs. $[8.0]-[24.0]$. Again, the field star locus is at the origin. This diagram is particularly efficient at identifying ‘transition’ disk objects, those having little excess shortward of $8.0 \mu\text{m}$. A reddening vector of $A_K = 5$ is shown in both the IRAC and the IRAC-MIPS diagrams.

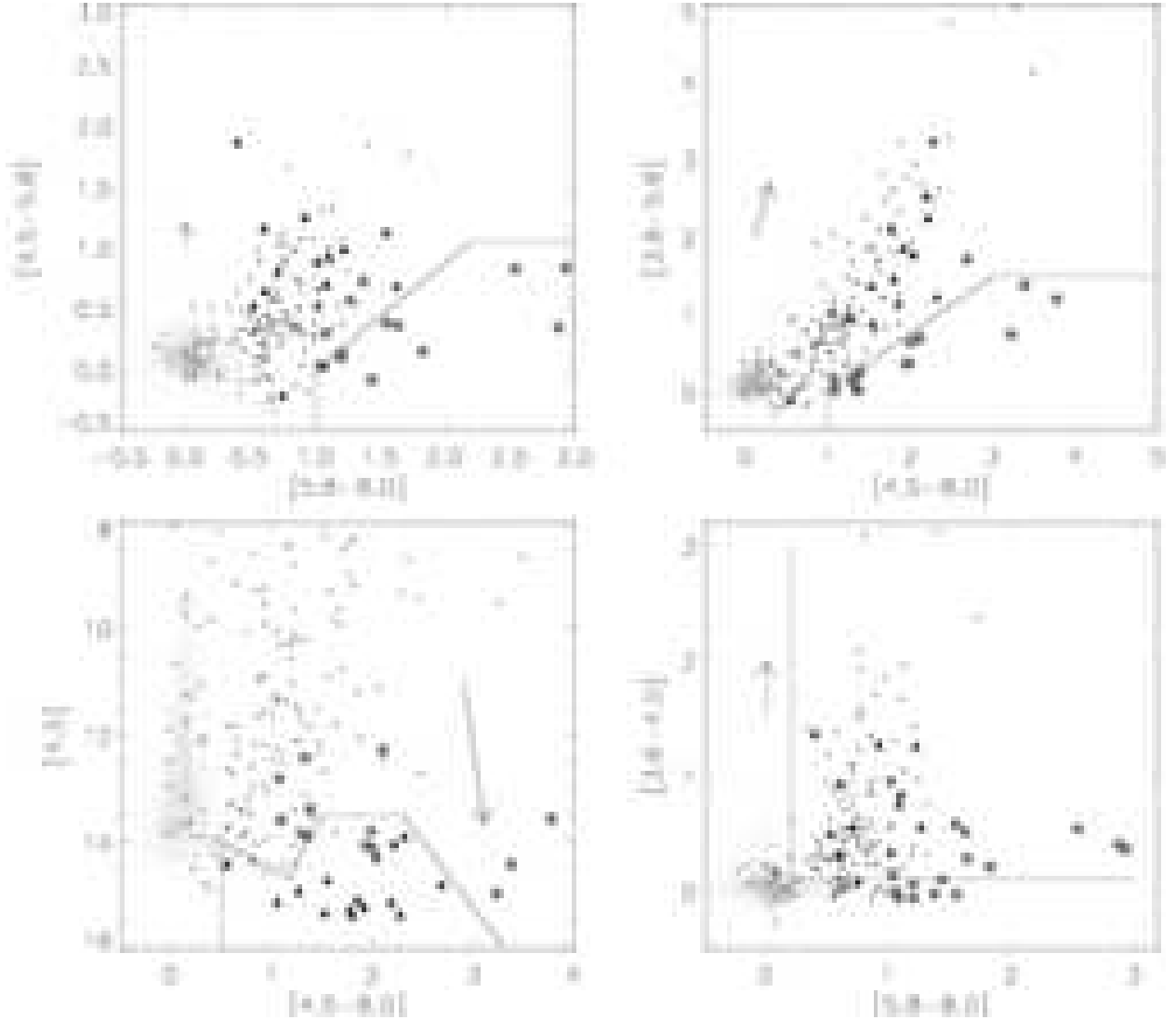


Fig. 5.— The above diagrams show the color and magnitude criteria used to remove likely star-forming galaxy and AGN contamination (Gutermuth et al. submitted). The grey dots are all sources with uncertainties < 0.2 mag in the relevant bands, the small squares are the YSOs, the large grey squares are sources selected as PAH-rich star-forming galaxies, and the black triangles are sources selected as AGN. The $[4.5] - [8.0]$ vs. $[5.8] - [8.0]$ (*above left*), $[3.6] - [5.8]$ vs. $[4.5] - [8.0]$ (*above right*), and $[3.6] - [4.5]$ vs $[5.8] - [8.0]$ (*bottom left*) diagrams are used to find the star-forming galaxies. In these cases, the lines show the criteria used to identify the star-forming galaxies. The AGN show colors much more similar to the YSOs and are instead identified by their faintness. The magnitude criteria used to find AGN is shown as a line in the $[4.5]$ vs. $[4.5 - [8.0]$ color-magnitude diagram. The IRAC color-color diagram (*bottom right*) is used to select out pure photospheres and stars contaminated by nebulosity. Excess sources have colors $> 1\sigma$ beyond $[3.6] - [4.5] > 0.1$ and $[5.8] - [8.0] > 0.2$. A $5 A_K$ reddening vector, from Flaherty et al.(2006), is overlaid on each plot.

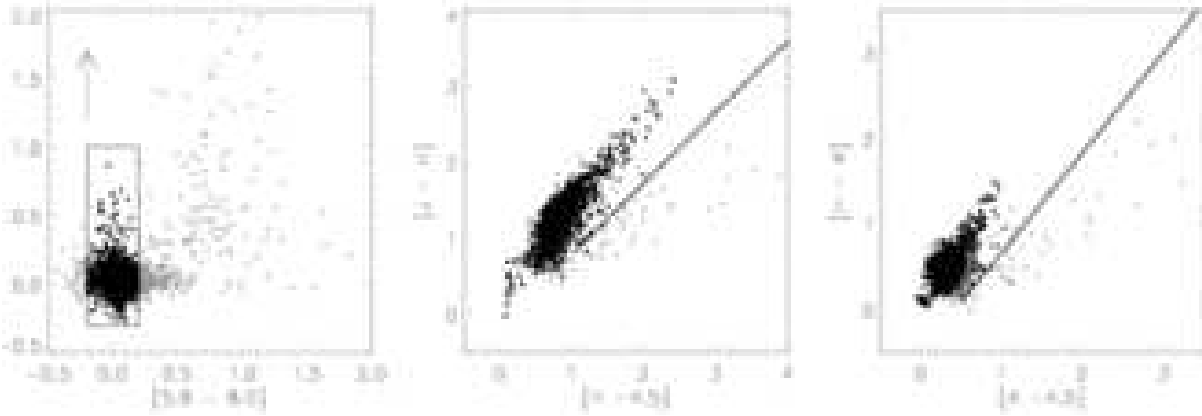


Fig. 6.— These figures illustrate the method used to establish the locus of reddened stellar photospheres on the IRAC-2MASS color-color diagrams. Only data with uncertainties 0.1 mag or less in all IRAC and 2MASS bands were plotted. The displayed reddening law was derived from this data by Flaherty et al. (2007). In each diagram, the black dots are the selected reddened photospheres, while the grey dots are the sources which show infrared excesses or large photometric scatter. Left: The IRAC [3.6] - [4.5] vs. [5.8] - [8.0] color-color diagram was used to select stars which do not show infrared excesses in the IRAC bands. The square indicates the location of the field star locus on this color-color plot. The reddening vector is for an $A_K = 5$. Middle: The black dots show the locus of reddened stellar photospheres plotted on the $J - H$ vs. $H - [4.5]$ color-color diagram. The reddening vector serves as our adopted dividing line between reddened photospheres and stars with infrared excesses; sources more than 1σ to the right of this vector are identified as having an infrared excess. Three sources out of the 1625 are misidentified as excess as their IRAC [3.6]-[4.5] vs [5.8]-[8.0] colors show them to be pure photospheres without infrared excess. Right: The distribution of reddened photospheres on the $H - K$ vs. $K - [4.5]$ color-color diagrams. Again, the displayed reddening vector is our adopted dividing line between pure photospheres and stars with infrared excesses. One source out of 1625 is misidentified as an excess as its IRAC colors are indicative of a pure photosphere.

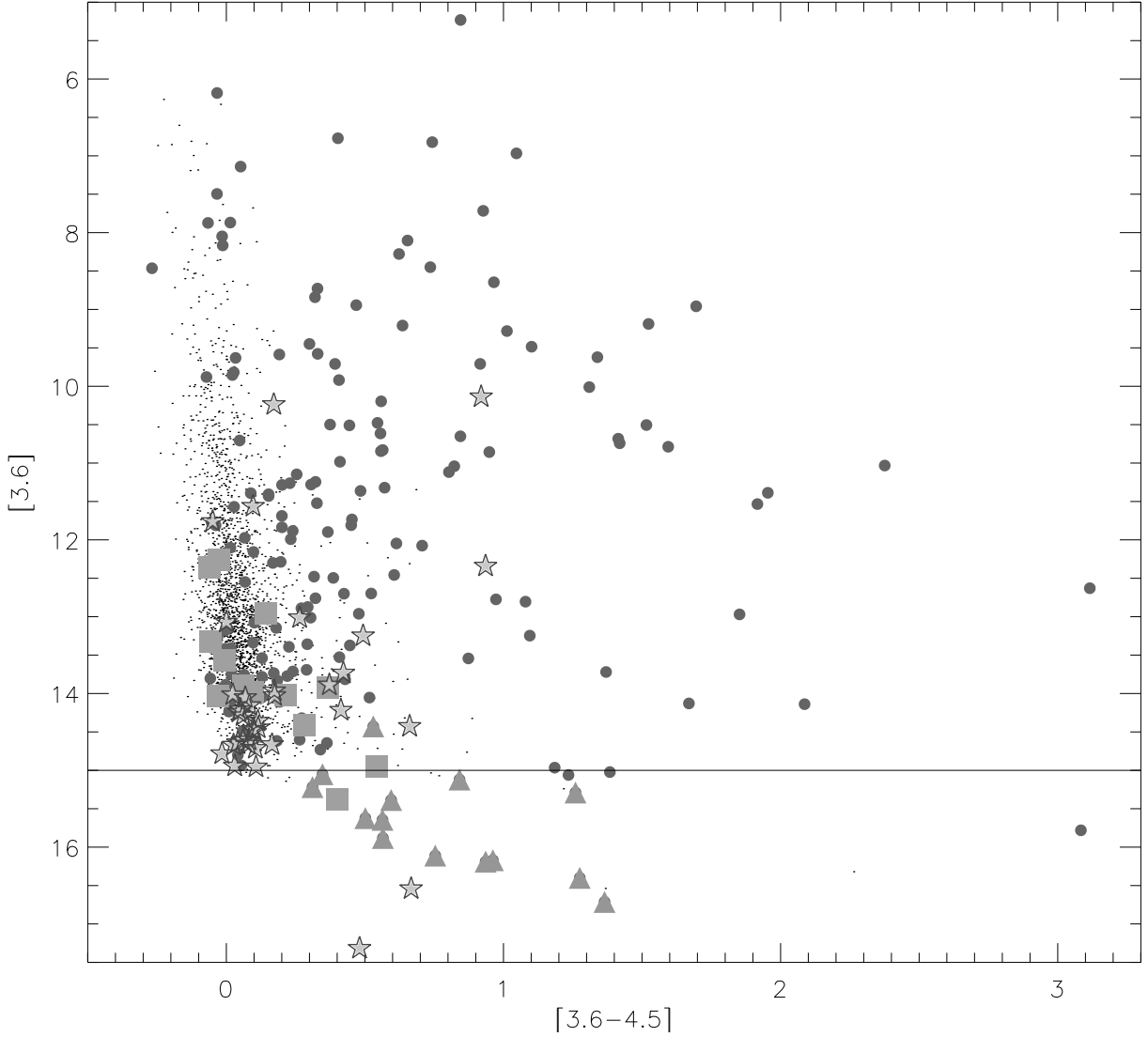


Fig. 7.— The distribution of YSOs and extragalactic contamination in the [3.6] vs. [3.6]-[4.5] color-magnitude diagram. The detections with photometric uncertainties < 0.2 mag in the overlap field are plotted as dots, with the 229 candidate YSOs overplotted in dark grey circles. A majority of the identified YSO sources have uncertainties < 0.2 mag in these two bands. While the star-forming galaxy contamination (light grey squares) have magnitudes similar to YSOs, they can be distinguished by their colors. In contrast, the AGN (light grey triangles) have colors similar to YSOs, but all lie in the region below a magnitude of 15 at $3.6 \mu m$. The stars represent those YSOs that do not possess full four band IRAC detections; we consider all of these sources with $m_{3.6} < 15$ to be contamination.

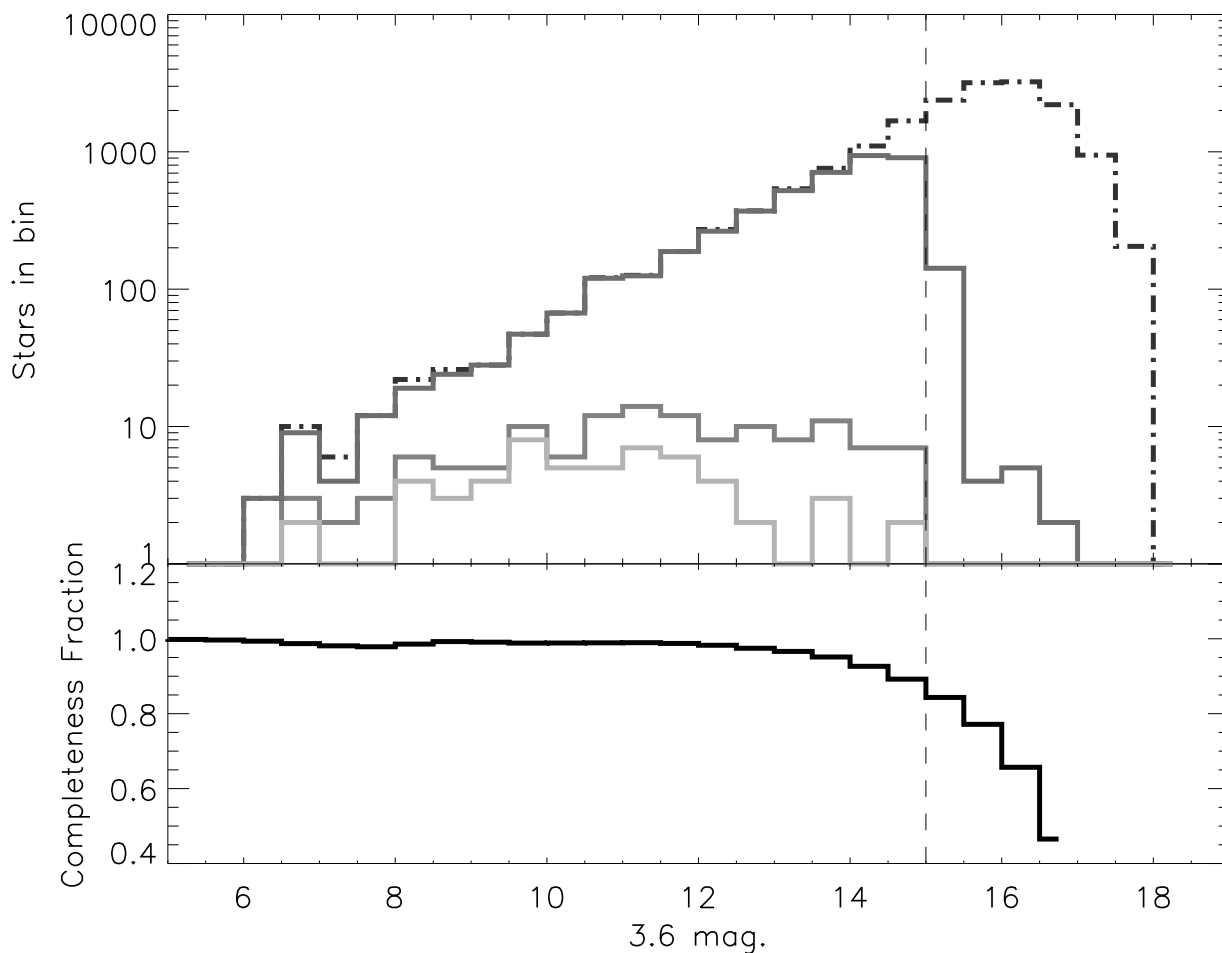


Fig. 8.— The top panel shows the histogram of all the photometry with a detection at $3.6 \mu\text{m}$, by magnitude, as a black dashed line. Overplotted are those sources with detections in the multiple bands needed to place them on the color-color diagrams used to select IR-excess sources, as shown by the upper gray line. The lower gray line plots the detections that were selected as YSOs in the final catalogue. The light gray line shows the subset of the identified YSOs that were detected in X-rays, note that the X-ray observations covered a smaller field than the IR observations. The bottom panel plots the fraction of artificial stars recovered as a function of their magnitude for the $3.6 \mu\text{m}$ IRAC data.

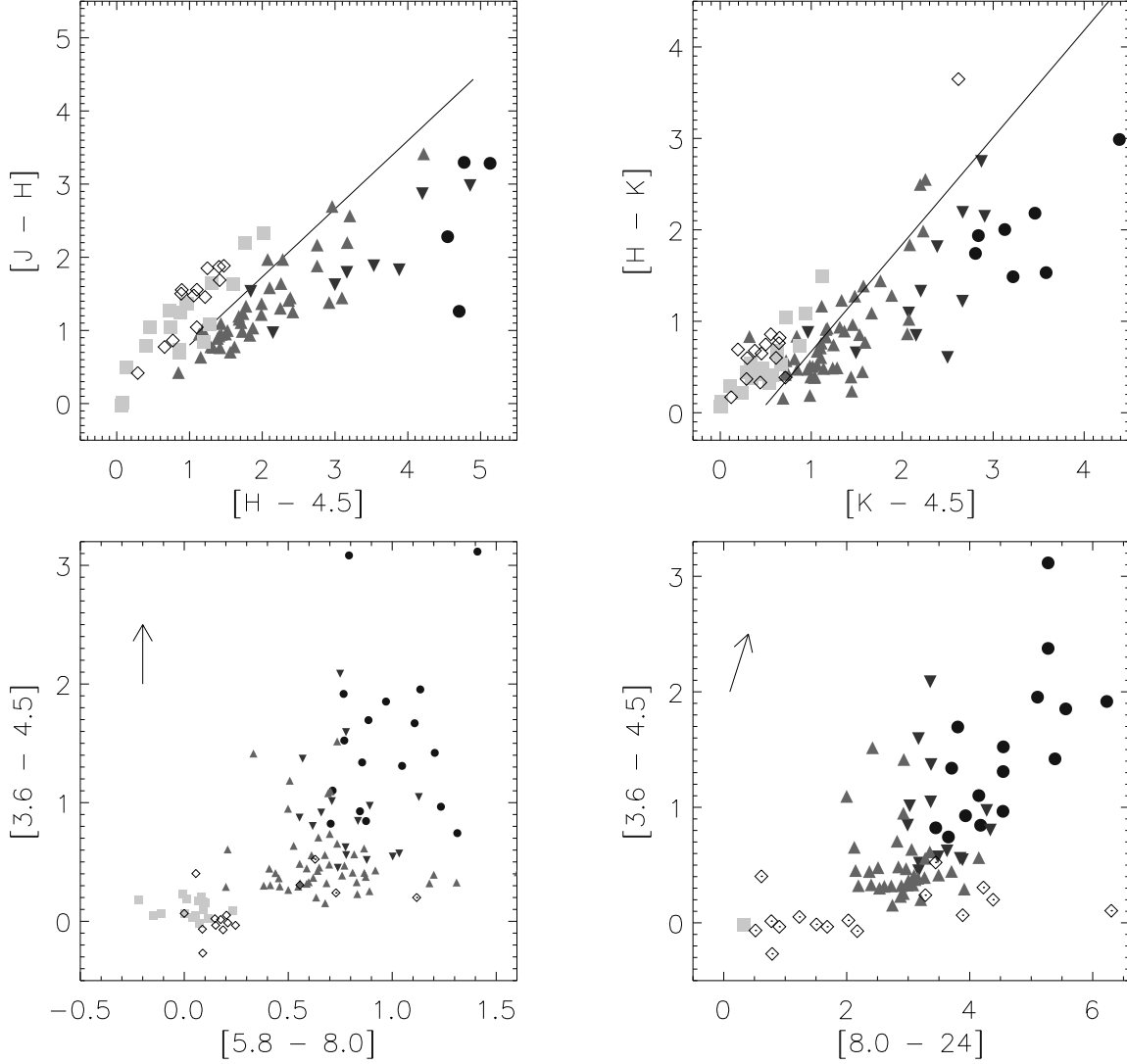


Fig. 9.— The same four diagrams as Fig. 4, this time indicating the positions of the young stellar objects identified in our analysis. Black circles mark the class 0/I objects, inverted dark grey triangles mark the flat spectrum sources, mid-grey triangles indicate the class II objects, while light grey squares show the X-ray identified class III sources. The transition disk objects are marked with clear diamonds. On the IRAC and IRAC-MIPS color-color diagrams some of the class II and transition disk stars appear to fall in the wrong region of the diagram for their class. An examination of the dereddened SEDs of these sources shows that their positions on the color-color diagrams have been shifted by reddening.

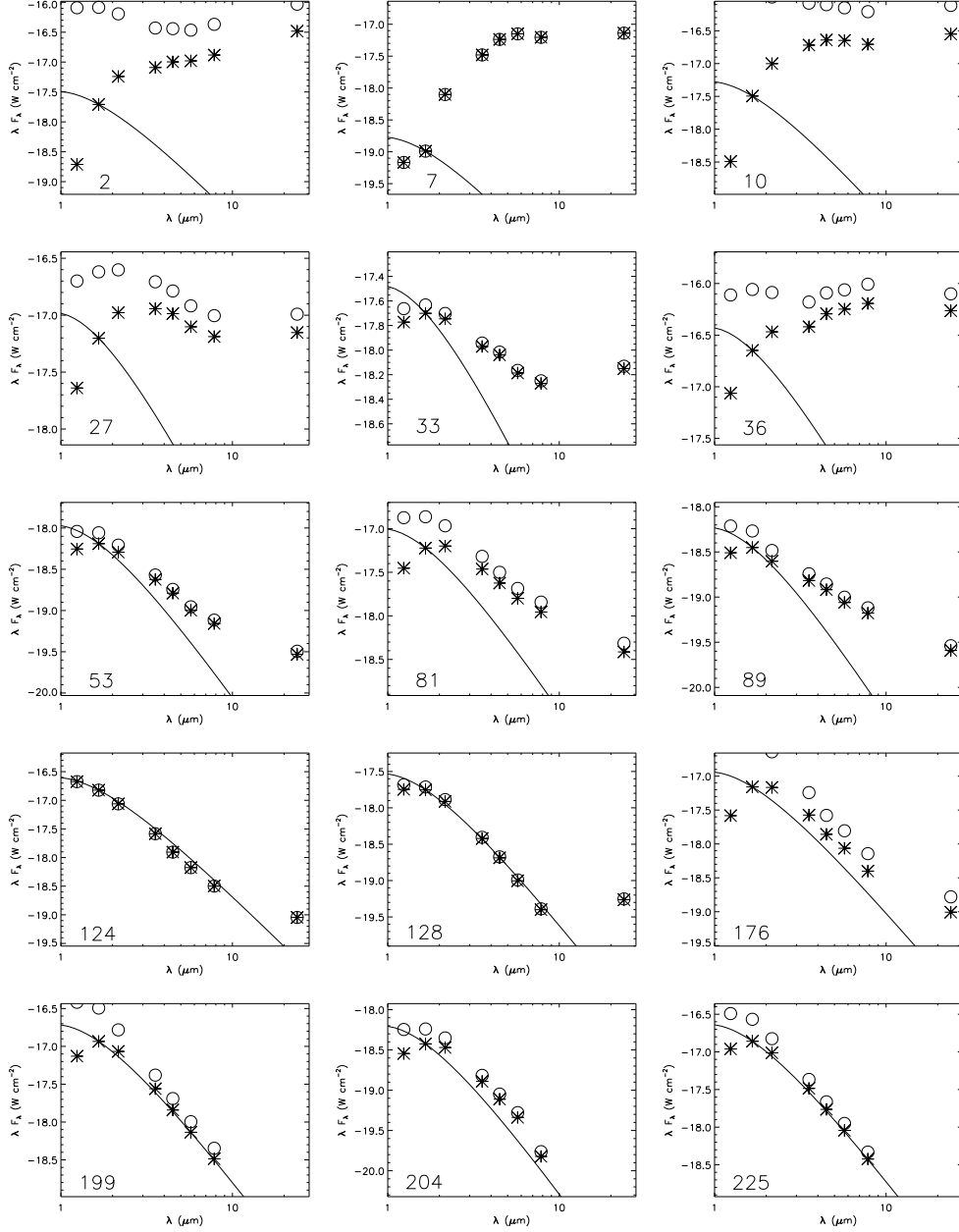


Fig. 10.— SEDs showing three typical examples of each evolutionary class in descending order: class 0/I, flat spectrum, class II, transition disks, class III. The circles show the measured fluxes, the asterisks the dereddened fluxes. The solid line is a 4000 K blackbody scaled to match the H -band flux.

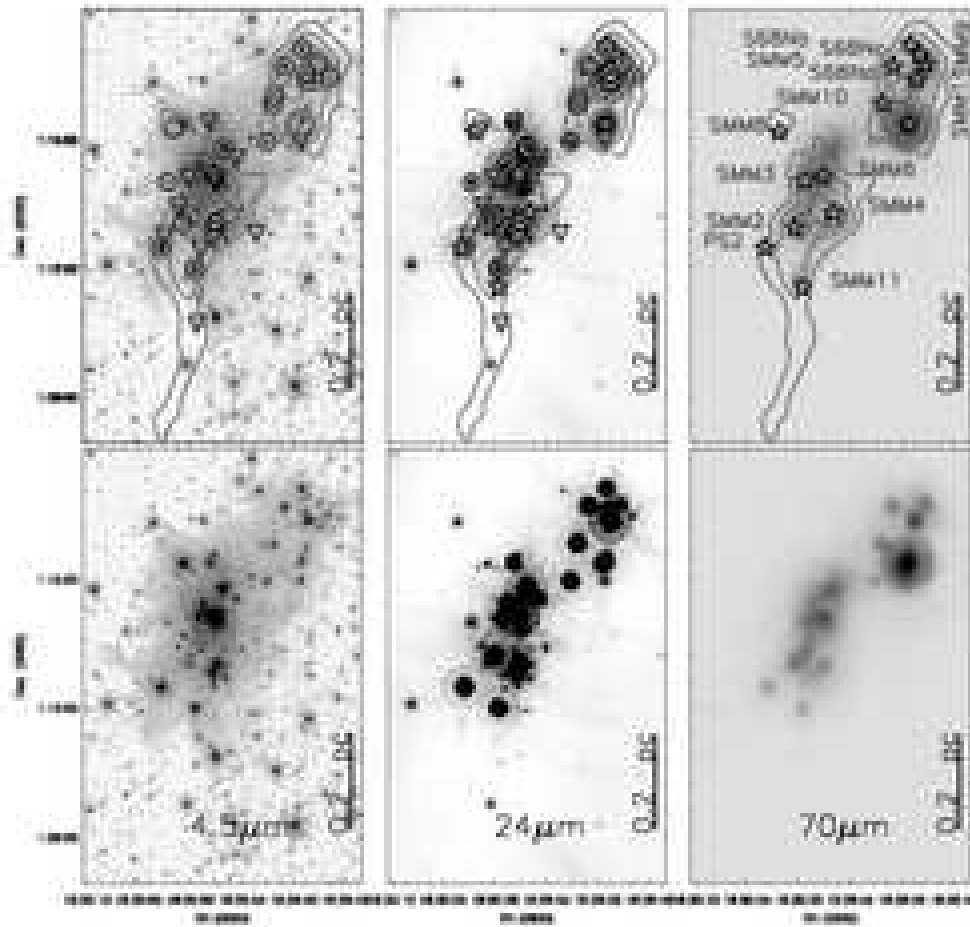


Fig. 11.— *Above*: Three grey-scale images of the Serpens Core, right to left: IRAC Ch.2, $4.5 \mu\text{m}$, MIPS $24 \mu\text{m}$, and MIPS $70 \mu\text{m}$. These are overlaid with contours from the $850 \mu\text{m}$ SCUBA data (Davis et al. 1999), at levels of [3%, 8%, 20%, 30%, 35%] of the peak flux. The asterisks mark the locations of the identified (sub)mm sources in the region, c.f. Table 6. Class I (circle) and Flat Spectrum (inverted triangle) YSOs are also shown. *Below*: The same three greyscale images shown without overlays.

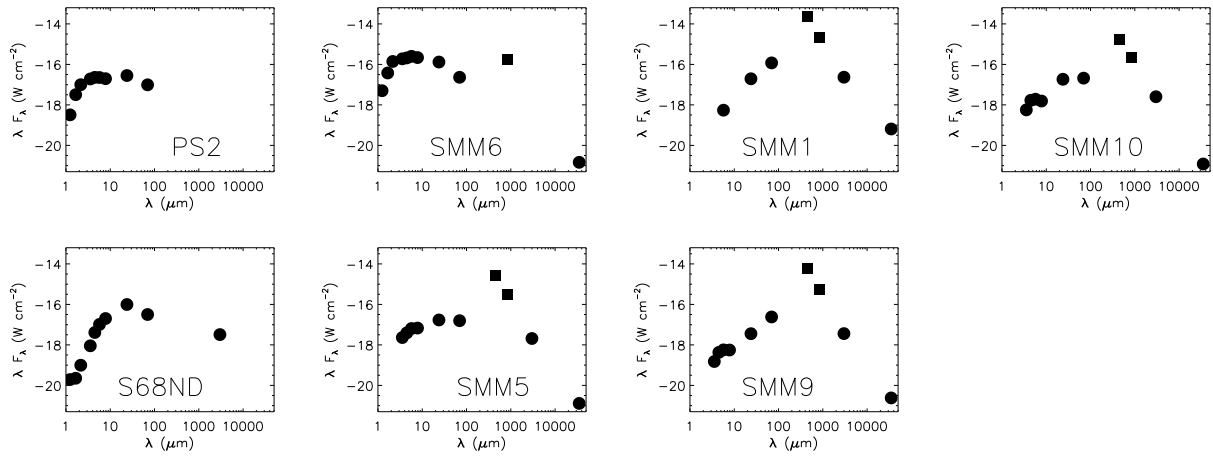


Fig. 12.— Spectral Energy Distribution of seven cluster members detected at $70\mu\text{m}$, with 3 mm and 3.5 cm data points plotted where available (Eiroa et al. 2005; Williams & Meyers 2000). The black squares indicate the peak flux per beam at 450 and 850 μm from Davis et al. (1999).

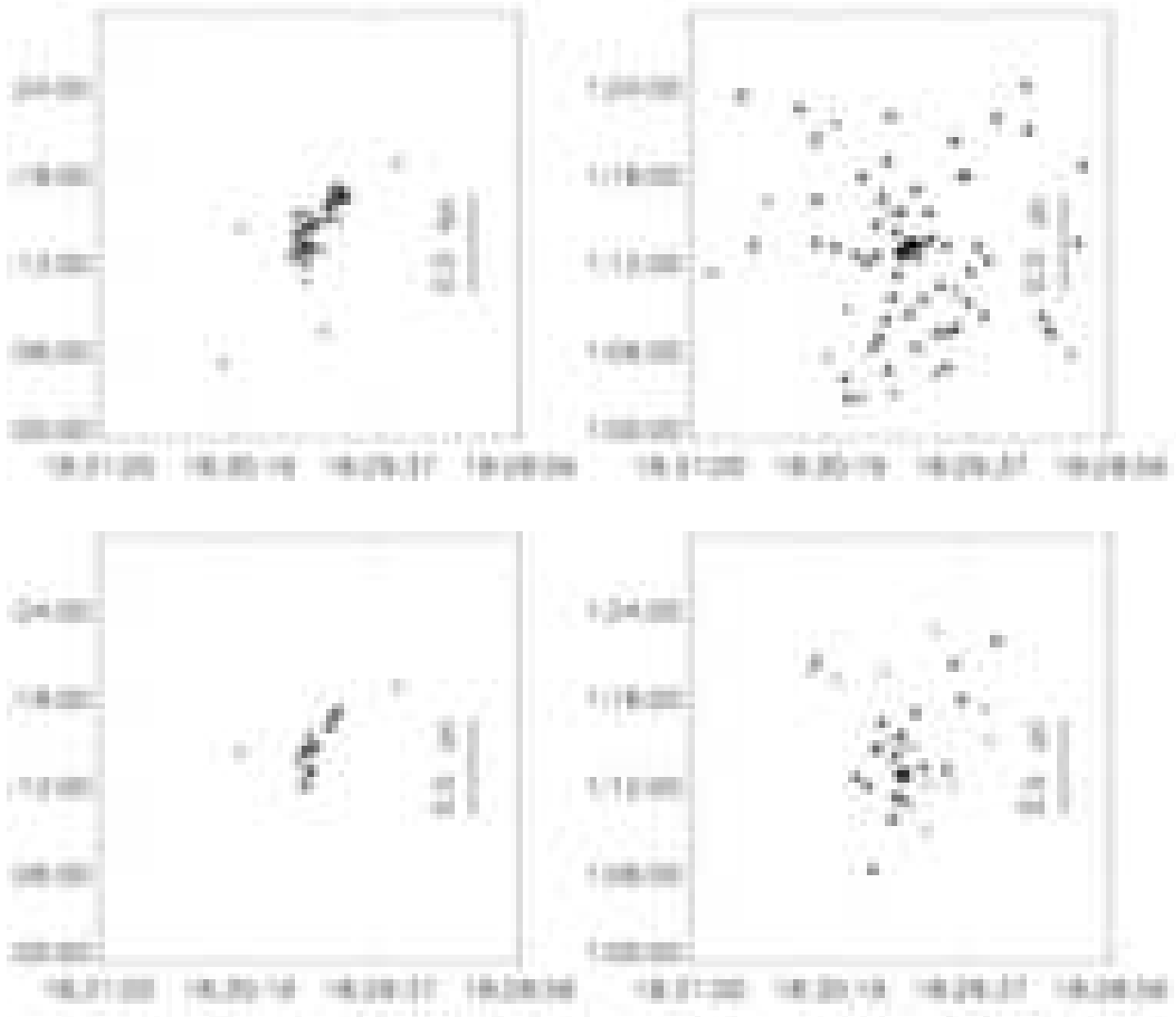


Fig. 13.— *Above:* The spatial distribution of the various classes of YSOs in the Serpens cloud core. *Upper Left:* Class I and flat spectrum sources, in circles and inverted triangles respectively. *Upper Right:* Class II (triangles) and transition disk members (diamonds). *Lower Left:* X-ray selected sample of class I and flat spectrum objects. *Lower Right:* X-ray selected sample of the class II, transition disk, and class III members (shown by squares). The dense clustering of the class I and flat spectrum sources can be seen, over the more widely dispersed class II and later members. Note: the extent of the IRX-field is smaller than the IR-field, as shown in Fig. 3.

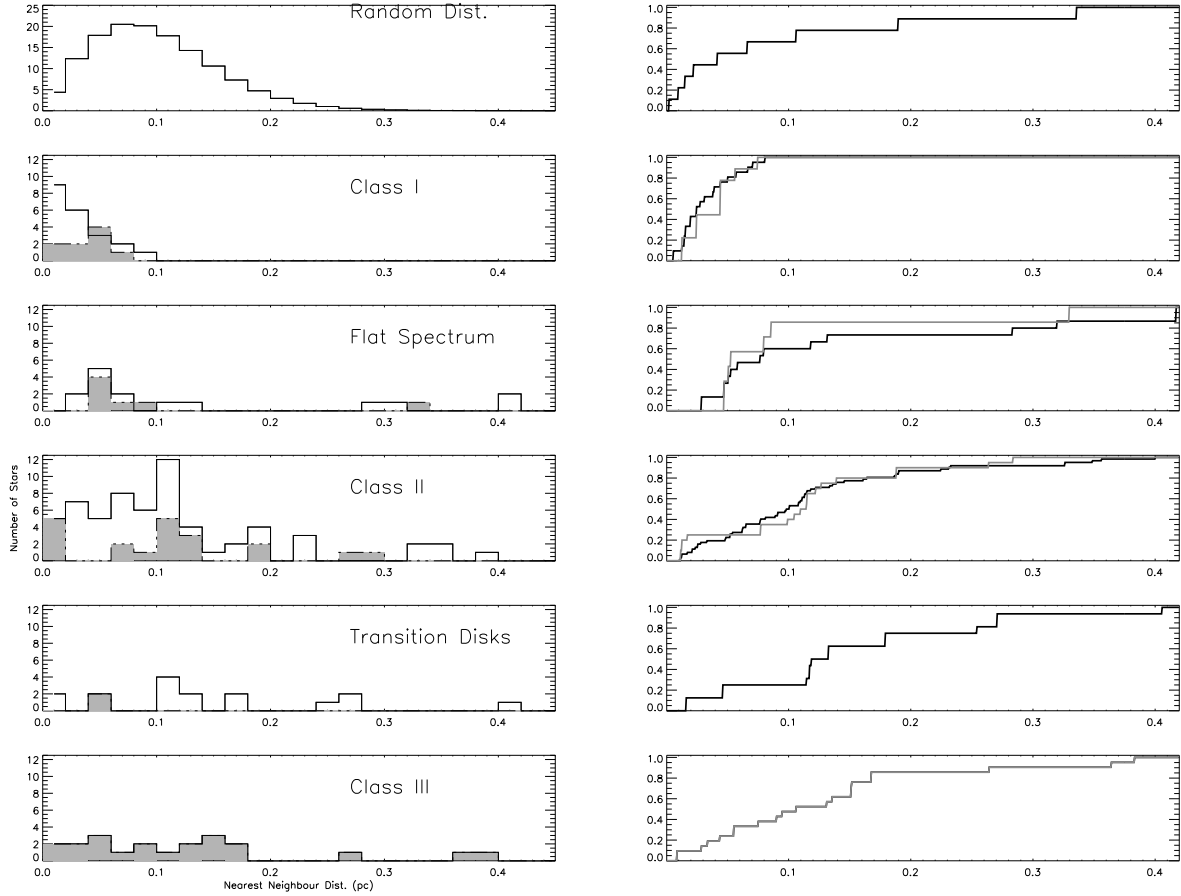


Fig. 14.— *Left:* Differential distribution of nearest neighbour distances by class for the identified YSOs (solid line), the shaded region gives the differential distribution of nearest neighbour distances by class for the X-ray selected sample of YSOs. The protostellar sources are densely clustered, with a wider distribution for the stellar sources. The top plot is the nearest neighbour distances for a random distribution. *Right:* Cumulative distribution of nearest neighbour distances by class for the identified YSOs, the grey line gives the X-ray sources. The top plot is the cumulative plot of a random distribution. A Kolmogorov-Smirnov probability shows the class I distribution to be different from the class II or class III distributions, and that the class II and class III distributions are statistically similar to the random distribution.

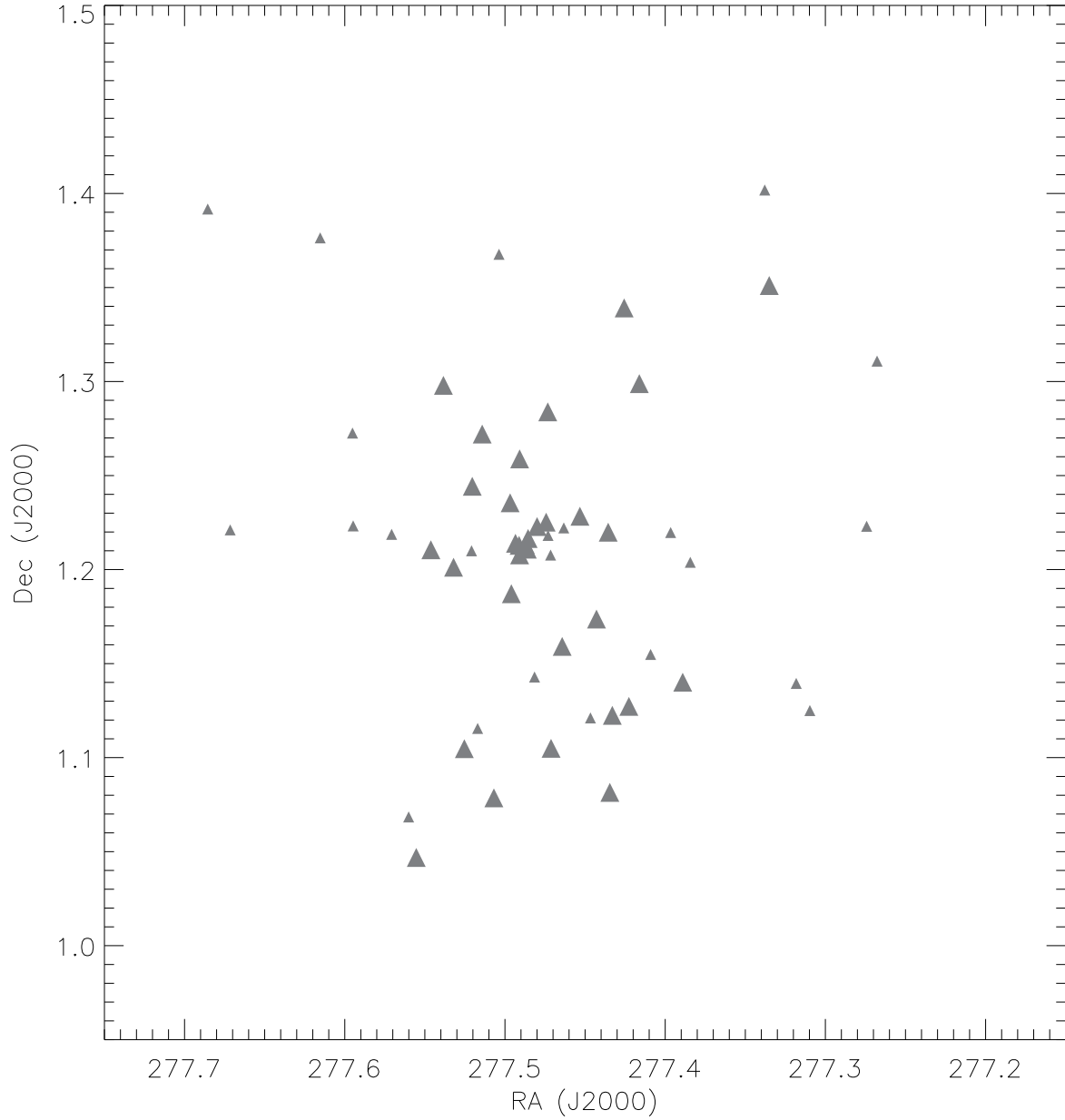


Fig. 15.— Spatial Distribution of the class II sources in the Serpens cluster. The larger symbols represent the sources with dereddened K-band magnitude brighter than 12.5, the smaller represent the sources with K-band magnitude fainter than 12.5. The two have similar distributions, indicating a similar formation mechanism for the two groups.

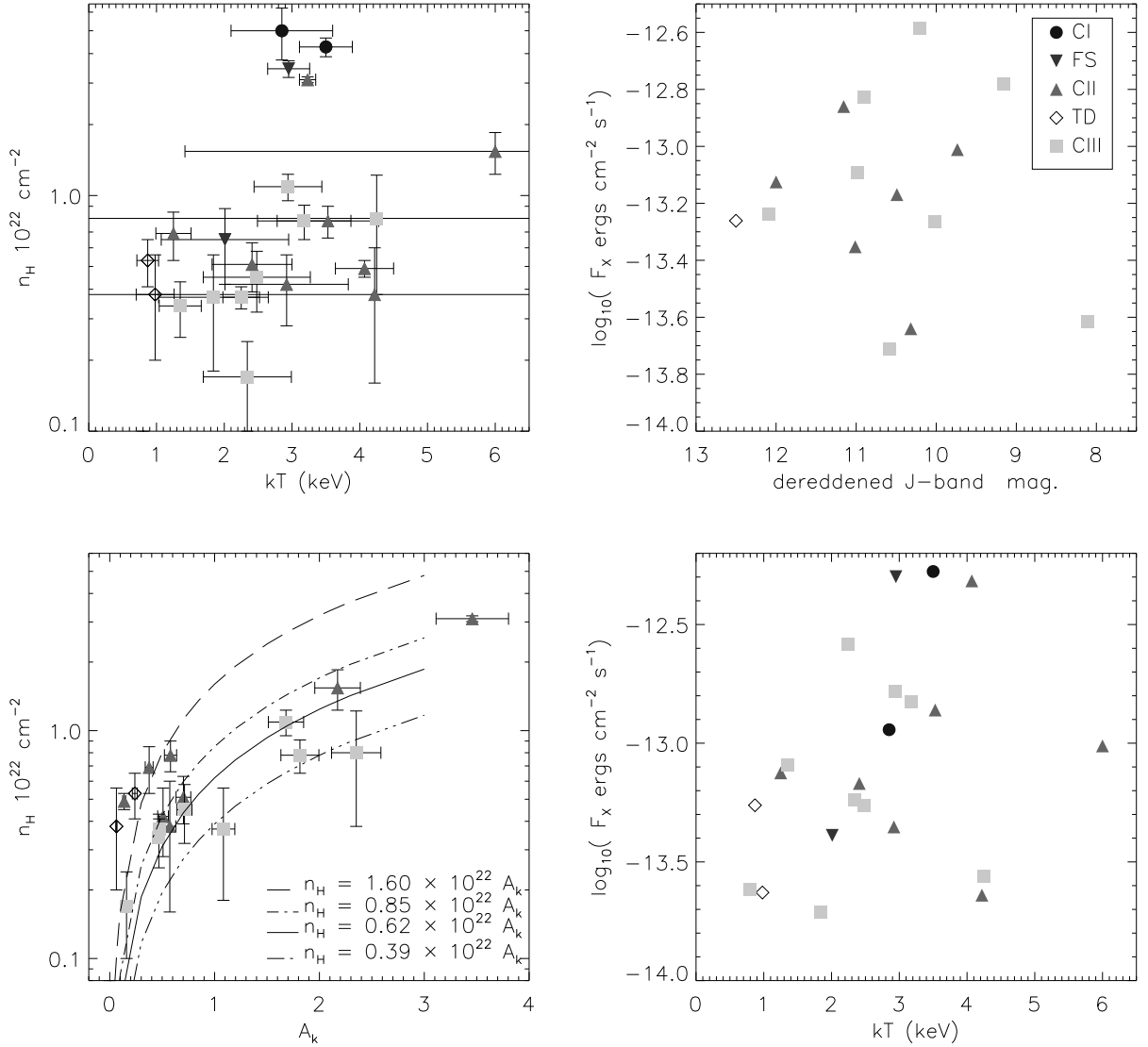


Fig. 16.— *Above left (a)*: Plasma temperature against Hydrogen column density. The class 0/I and flat spectrum sources show higher N_H , consistent with the presence of an infalling envelope. The class II and III sources do not exhibit a trend in kT with N_H . *Above right (b)*: X-ray luminosity against dereddened J-band luminosity. A slight trend of increasing flux with increasing luminosity is present. *Below left (c)*: Hydrogen number density against extinction at K-band. The gas density was calculated from the *Chandra* data. The curves indicate the standard N_H/A_K ratio, which does not hold for $A_K > \sim 1.5$, and the ratio calculated from these data. *Below right (d)*: The plasma temperature plotted against the log of the X-ray luminosity. A slight trend of increasing flux with kT is present. The symbols are as follows: class 0/I, circle; flat spectrum, inverted triangle; class II, triangle; transition disk, diamond; class III, squares.